

Experimental and numerical study of the shear layer instability between two counter-rotating disks

By F. MOISY¹, O. DOARÉ¹, T. PASUTTO¹,
O. DAUBE² AND M. RABAUD¹

¹Laboratoire FAST, Bât. 502, Campus Universitaire, F-91405 Orsay Cedex, France

²CEMIF/LME, Université d'Evry, 40 Rue du Pelvoux, F-91020 Evry Cedex, France

(Received 5 September 2003)

The flow between two counter-rotating disks enclosed by a cylinder is investigated experimentally and numerically, for radius-to-height ratio $\Gamma = R/h$ ranging from 2 to 21. The steady axisymmetric basic flow presents an internal shear layer that separates two regions of opposite azimuthal velocities, which is prone to an azimuthal symmetry breaking. For sufficiently large rotation ratio, this free shear layer is strengthened by the presence of a stagnation circle on the slower disk, which is characterized systematically by numerically solving the axisymmetric Navier–Stokes equations. The instability of the internal shear layer is investigated experimentally by means of visualization and particle image velocimetry. The associated pattern is a combination of a sharp-cornered polygonal pattern, as observed by Lopez *et al.* (2002) at low aspect ratio, surrounded by a set of spiral arms, first described by Gauthier *et al.* (2002) in the case of high aspect ratio. The spiral arms result from the interaction of the shear layer instability with the Ekman boundary layer over the faster rotating disk. Stability curve and critical modes are experimentally measured for the whole range of aspect ratios, and are found to compare well with the numerical simulations of the three-dimensional time-dependent Navier–Stokes equations over an extensive range of parameters. From the measurement of a local Reynolds number based on the shear layer thickness, evidence is given that a shear layer instability, with only weak curvature effect, is responsible for the observed patterns. This scenario is supported by the observed onset modes, which scale as the shear layer radius, and by the measured phase velocities.

1. Introduction

The flows between rotating disks, or von Kármán (1921) swirling flows, occur in a variety of situations, from industrial to geophysical applications. The fundamental problem of the basic flow in the infinite disk case has been reviewed by Zandbergen & Dijkstra (1987). The stability of these flows has been addressed since a long time, mostly in the rotor-stator configuration, i.e. between one rotating and one stationary disks.

Of practical interest for laboratory experiments is the case of finite disks, for which no similarity solutions exist. The nature and the stability of the flow then strongly depends on the radius-to-height ratio, $\Gamma = R/h$, and the rotation ratio, $s = \Omega_b/\Omega_t$ (t and b refer to the top and bottom disks). Most of the studies deal with the rotor–stator configuration, $s = 0$, and it is only recently that the intermediate cases, $-1 < s < 1$, are addressed experimentally and numerically (Lopez 1998; Lopez *et al.* 2002; Gauthier *et al.* 2002;

Nore *et al.* 2003*a, b*; Marques *et al.* 2003). Other parameters may also be taken into account, such as the presence of a central hub or the end condition of the sidewall; these extra parameters are of practical importance, for instance in hard disk systems, for which $\Gamma \sim O(10)$ and $s = 1$ (Humphrey, Schuler & Webster 1995), or turbomachines. The quasi-solid body rotation limit, $s \approx 1$, is of great importance in geophysical flows (Stewartson 1953; Hide & Titman 1967; Fröh & Read 1999). In the limiting case of very long tube, $\Gamma \ll 1$, the rotating disk has a vanishingly small effect far from it and the flow is dominated by the wall condition. The cases of intermediate aspect ratio, $\Gamma \sim O(1)$, and flat cavities, $\Gamma \gg 1$, are much richer, although very different from each other.

The investigation of the flow in rotor-stator $\Gamma \sim O(1)$ cavities has been mainly motivated by the experimental observation of a vortex breakdown in the form of a recirculatory bubble by Escudier (1984). The axisymmetry breaking of the basic flow gives rise to rotating waves, analysed in detail by Gelfgat *et al.* (2001), Blackburn & Lopez (2002) and Serre & Bontoux (2002) for $\Gamma < 1$. The more symmetric case of exact counter-rotation, $s = -1$, with stationary sidewall also received considerable interest. The complete scenario of bifurcations for an aspect ratio $\Gamma = 1/2$ has been numerically investigated by Nore *et al.* (2003*a*). They have shown that the basic state becomes unstable through a Kelvin-Helmholtz instability of the equatorial free shear layer, giving rise to one or two radial co-rotating vortices. Extension of this study for Γ between $1/3$ and 2 has been recently carried out by Nore *et al.* (2003*b*).

The limit of very flat cavity, $\Gamma \gg 1$, has been investigated experimentally in the rotor-stator configuration by Cros & Le Gal (2002) at $\Gamma \approx 64$. In this limit, no separated boundary layers appear even at large shear, and the flow remains of torsional Couette type. Instabilities in the form of turbulent spirals, similar to the turbulent spots observed in the plane Couette or Taylor-Couette flows, are reported by these authors.

For thicker cavities, $\Gamma \sim O(10)$, the recent experimental studies have mainly focused on the boundary layer instabilities in the rotor-stator case (Gauthier, Gondret & Rabaud 1999; Schouveiler, Le Gal & Chauve 2001), further characterized numerically by Serre, Crespo del Arco & Bontoux (2001). Two classes of instability are observed, axisymmetric propagating vortices and positive spirals. Extension of these studies to differential rotation of the disks has been performed by Gauthier *et al.* (2002) for $\Gamma = 20.9$. It was shown that the corotating and weak counter-rotating flows only weakly affect the properties of these boundary layer instabilities, like linearly shifting the instability thresholds or the onset modes.

The counter-rotating regime of flat cavities with higher rotation ratio appears to be much richer: in addition to the above mentioned boundary layer instabilities, it has been recently recognized that this flow also shows free shear layer instability. The reason for this new instability is that the topology of the counter-rotating flow drastically changes for sufficiently large rotation ratio, evolving towards a two-cell recirculation flow with a stagnation circle on the slower disk. This property was first described experimentally and numerically by Dijkstra & van Heijst (1983) for $\Gamma = 14.3$, and further characterized by Lopez (1998) for $2 \leq \Gamma \leq 8$ from axisymmetric numerical simulations. The inward boundary layer on the slower disk gets detached due to this stagnation circle, leading to an internal shear layer that separates two regions of opposite azimuthal velocities, along which the velocity is jet-like. This free shear layer may be unstable to azimuthal disturbances, as first conjectured by Lopez (1998).

Detailed investigation of the resulting instability by means of dye visualization and three-dimensional numerical simulations, restricted to $\Gamma = 2$ and $\Omega_t h^2 / \nu = 250$, has been performed by Lopez *et al.* (2002). These authors observed patterns of wavenumber 4 and 5, in the form of ‘funnel-like’ vortices, that they attributed to an instability of

the internal shear layer. At the same time, for a very different aspect ratio $\Gamma = 20.9$, Gauthier *et al.* (2002) reported a new instability pattern of wavenumber 9 to 11, in the form of a set of spiral arms. This new pattern received the name of ‘*negative*’ spirals, because they roll up to the center in the direction of the slower disk. Although the morphology of the funnel-like vortices and the negative spirals patterns strongly differ, the issue of a possible continuity between them was first raised by Gauthier *et al.* (2002), and addressed experimentally by Moisy, Pasutto & Rabaud (2003). Further numerical simulations at low aspect ratio were performed by Marques, Gelfgat & Lopez (2003), focusing on the codimension-3 Hopf bifurcation that takes place at $\Gamma \approx 1.79$ between the modes 4 and 5.

The influence of the curvature and rotation on the stability of internal shear layers received considerable interest (Dolzanskii, Krymov & Manin 1990). In addition to Kelvin-Helmholtz instability, also present for linear non-rotating shear layers, centrifugal effect may occur, with a stabilizing or destabilizing effect (Yanase *et al.* 1993; Liou 1994; Otto, Jackson & Hu 1996). The extreme case where rotation dominates the dynamics (small Rossby number) plays a central role in geophysical flows. In this context, shear instabilities fall into the class of barotropic mechanisms. After the pioneering study of Hide & Titman (1967), laboratory experiments aiming to model such instability are based on the differential rotation of a disk in a rapidly rotating tank (Niino & Misawa 1984; Konijnenberg *et al.* 1999) or a cylindrical split-annulus tank (Früh & Read 1999). These experiments focus on weak shear compared to the background rotation, and show patterns in the form of circular chains of eddies, with complex nonlinear mode selection and eddy clustering. Closer to our experiment, Rabaud & Couder (1983) have investigated the stability of a two-dimensional forced circular shear layer in a split-annulus tank without background rotation, further studied numerically by Chomaz *et al.* (1988) and Bergeron *et al.* (2000). Although in these experiments the rotation only weakly affects the shear layer instability, patterns in the form of circular chains of eddies are observed as well, the number of which decreasing as the Reynolds number is increased.

The purpose of this paper is to analyse in details the shear layer instability in the counter-rotating flow for a range of aspect ratio Γ between 2 to 20.9. We restrict ourselves to the situation where the boundary layers remain stable: axisymmetric propagating vortices and positive spirals are not considered here. The outline of the paper is as follows: section 2 briefly presents the experimental set-up and the two investigation techniques, namely visualization and particle image velocimetry (PIV). The numerical methods are summarized in § 3. The steady axisymmetric basic flow is described in § 4, with special attention paid to the existence domain of the two-cell recirculating flow. Instability patterns and onset curves are described in § 5 from PIV measurements and numerical simulations. In § 6 the instability is characterized in terms of a local Reynolds number based on the internal shear layer. Systematic measurements of the onset modes and phase velocities are presented, and are shown to compare well with a classical Kelvin-Helmholtz instability mechanism. Some concluding remarks are finally offered in section 7.

2. Experimental set-up

2.1. Experimental cell

The experimental cell, sketched in figure 1, is adapted from the one of Gauthier *et al.* (2002) to allow for lateral visualisation and lighting. It consists of a rotating cylinder of radius $R = 140$ mm, in which a disk of same radius located at the bottom of the cavity rotates at a different speed. The cylinder and its upper cover (top disk) are made of Plexiglas,

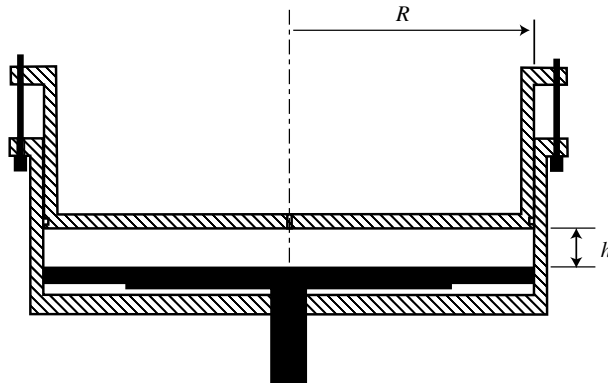


FIGURE 1. Experimental cell. The cylinder (crosshatched regions), made of transparent Plexiglas, rotates with angular velocity Ω_t , while the bottom disk (black) rotates in the opposite sense with angular velocity Ω_b .

to allow for visualizations from above and from the side, while the bottom disk is made of black painted brass to improve the visualization contrast. The thickness of the cell h can be varied from a few millimetres to 7 cm, using wedges between the upper disk and the cylinder rim.

The angular velocities of the top and bottom disks, Ω_t and Ω_b , can be set independently, from 0 to 10 rad s^{-1} . Since we are only concerned with the counter-rotation flow in the present paper, there is no ambiguity in the sign of the angular velocities, which are taken positive. The upper disk is the faster one, $\Omega_t \geq \Omega_b$, throughout the paper, except in section 5.2 where the influence of the rotating sidewall is investigated. For both experimental and numerical visualisations, the flow is seen from above, the upper disk rotates anticlockwise while the bottom one rotates clockwise.

Water-glycerol mixture and silicone oils have been used as working fluids, allowing to span a range of kinematic viscosity between 1.0×10^{-6} and 50×10^{-6} m^2/s at 20°C . Viscosity changes due to temperature drift during experiments (about 2% per degree for both glycerol and silicone oils) were controlled, and all the uncertainties finally lead to an accuracy of 3% in the determination of the Reynolds numbers.

2.2. Dimensionless numbers

The flow is characterized by three dimensionless numbers, two Reynolds numbers based on each disk velocity and the aspect ratio $\Gamma = R/h$. Since two lengthscales, R and h , are present in this geometry, freedom exists in the definition of the Reynolds numbers. The basic Reynolds numbers are here based on the cell thickness h ,

$$Re_i = \Omega_i h^2 / \nu, \quad (2.1)$$

where $i = b, t$ denotes the bottom and top disks. In the limit of very large Γ , the cell radius R has a vanishingly small influence on the flow and these Reynolds numbers Re_i are expected to be the relevant control parameters. In particular they allow to distinguish between separated and merged boundary layers situations. On the other hand, for flatter cavity $\Gamma \approx O(1)$, both R and h are relevant, so that the Reynolds numbers based on the thickness and the peripheral velocities,

$$\Gamma Re_i = \Omega_i R h / \nu, \quad (2.2)$$

are also of interest. In the present study, the Reynolds numbers Re_i are of order of 10 – 2000, and the aspect ratio Γ has been varied between 2 and 20.9.

In some cases, the use of the set of parameters (Γ, Re_t, s) , where $s = \Omega_b/\Omega_t = Re_b/Re_t$ is the counter-rotation ratio, is more convenient than (Γ, Re_t, Re_b) . Since we are only concerned with the counter-rotation case here, the ratio s is taken always positive. Note that this definition contrasts with the one adopted by Gauthier *et al.* (2002), where $s < 0$ were taken for the counter-rotating regime and $s > 0$ for the co-rotating regime.

2.3. Measurement techniques

Qualitative insight into the flow structure is obtained from visualization of the light reflected by anisotropic flakes seeding the flow. We make use of Kalliroscope[†] when the working fluid is water-glycerol mixture, and Iriodin[‡] when it is silicone oil. The flow is illuminated by a concentric circular light source, and pictures are obtained using a CCD camera located above along the disk axis. Although no direct information of the velocity field can be obtained from this method, quantities such as the wavelength or phase velocity of the structures can be extracted from the spatial variation of the reflected light (Savas 1985; Gauthier *et al.* 1998).

More quantitative measurements have been performed using a particle image velocimetry (PIV) apparatus[¶]. Small borosilicate particles, 11 μm in diameter, seeding the flow are used as tracer, illuminated by a laser sheet of thickness about 0.5 mm produced by a double pulsed Nd:Yag (25 mJ/pulse) and a cylindrical lens. Images are acquired with a double-buffer high resolution camera (12 bits, 1280×1024 pixels), synchronized with the laser at a rate of 4 frames pairs per second. The velocity fields are averaged over 4 successive individual fields, i.e. during 1 s, a value much lower than the characteristic timescale of the flow.

The structure of the axisymmetric basic flow in the meridional plane is obtained with a vertical laser sheet lighting. The cylindrical wall allows for undistorted pictures in the central part of the cell, $r \leq 0.7R$. The important out-of-plane azimuthal velocity component strongly constrains the time delay between the two successive frames, of order of 4 ms. A resolution down to 0.5×0.5 mm can be achieved, except near the disks where the important vertical gradient and out-of-plane velocity component prevent from resolving the boundary layers.

The bifurcated patterns are investigated using an horizontal laser sheet lighting between the two disks and the camera above. For these measurements, a sufficiently large disk separation h and a perfectly horizontal laser sheet are required due to the important vertical gradients. For these reasons, systematic measurements were only possible for low aspect ratio, $\Gamma = 3$ ($h = 46.7$ mm) and $\Gamma = 7$ ($h = 20$ mm), but some flow patterns have also been obtained up to $\Gamma = 14$ ($h = 10$ mm). Another important constrain arises from the important variability in the velocity, from mm/s near the center up to 10 cm/s in periphery, making difficult the choice of a unique window size for the PIV computations and time delay between the frames. Typical time delays of order of 30 ms are chosen for measurements near the centre, $r \leq 0.7R$, where the instability patterns essentially take place.

3. Numerical method

The numerical simulations of the three-dimensional flow between counter-rotating disks for various aspect ratios are carried out by numerically solving the time-dependent

[†] Kalliroscope Corporation, 264 Main Street, box 60, Groton, MA 01450, USA.

[‡] Iriodin: Pigments sold by Merck Corporation.

[¶] Flowmaster 3, LaVision GmbH, Anna-Vandenhoeck-Ring 19, D-37081 Goettingen, Germany.

Navier–Stokes equations. In addition, a linear stability analysis of the steady axisymmetric basic flow is also performed, in order to get a better insight into the nature of the azimuthal symmetry breaking and the onset modes.

A general methodology to numerically investigate flow instabilities has been developed by Gadoin *et al.* (2001), Daube & Le Quéré (2002), and Nore *et al.* (2003a). Only the main features of this methodology are reminded in this section. The approach is as follows:

- (i) The steady axisymmetric basic flow, which may be stable or unstable, is computed. This stage requires the use of a specific steady state solver.
- (ii) The full nonlinear Navier–Stokes equations are solved for the fluctuations around the basic flow.
- (iii) The linearized Navier–Stokes equations around the basic flow are possibly solved. For this purpose, several computational tools are used, which are based upon the use of the same spatial discretization, the details of which may be found in Barbosa & Daube (2001).

3.1. Spatial discretization

The different unknowns are first expanded in truncated Fourier series over N modes in the azimuthal direction. The coefficients of this expansion are then discretized in the (r, z) planes by means of mimetic finite difference operators (Hyman & Shashkov 1997):

- (i) A staggered, uniform or non uniform, grid in cylindrical coordinates (r, θ, z) is used. Noteworthy is the fact that the only unknown located on the axis $r = 0$ is the axial component ω_z of the vorticity.
- (ii) The first order differential operators divergence and curl are discretized by means of the Gauss and Stokes theorems written on elementary cells.
- (iii) The space \mathcal{H} of the discrete vectors and the space \mathbb{H} of the discrete scalar functions are equipped with inner products $\langle \cdot, \cdot \rangle_{\mathcal{H}}$ and $\langle \cdot, \cdot \rangle_{\mathbb{H}}$ derived from the \mathbb{L}^2 inner products of the continuum case. The discrete gradient operator is then defined as the negative adjoint of the discrete divergence operator with respect to these discrete inner products. The nonlinear terms are written as $(\nabla \times \mathbf{v}) \times \mathbf{v}$ and discretized such that $\langle \mathbf{v}, (\nabla \times \mathbf{v}) \times \mathbf{v} \rangle_{\mathcal{H}} = 0$, therefore ensuring kinetic energy conservation. As usual, they are computed in the physical space with the classical 3/2 rule.
- (iv) The second order differential operators are built as compounds of first order discrete operators, therefore ensuring that the Laplace operators are self adjoint. This fact, together with the use of a staggered grid, ensures that the discrete problem to be solved at each time step is well posed.

Since the discrete linear systems are solved by means of partial diagonalization techniques, using a uniform grid allows us to perform the involved change of basis by means of FFT routines instead of matrix–matrix products. Therefore, a uniform grid with 100 meshes in the z direction was found to be sufficient to study configurations with moderate aspect ratio, $\Gamma = 3$ and $\Gamma = 7$, whereas a non uniform grid in the z direction (with a mesh distribution defined by a hyperbolic tangent function) and a partially non uniform grid (refined near the outer wall) in the r direction was used for $\Gamma = 21$.

3.2. Computation of the basic flow

Since the computation of the steady axisymmetric basic flow is needed, even when it is unstable, the usual procedure which consists of obtaining steady state solutions by letting $t \rightarrow \infty$ in a time stepping code must be rejected in favor of a Newton–Raphston method. The main drawback of this approach is that the Jacobian matrix of the Navier–Stokes operator is huge and ill-conditioned. To overcome these difficulties, we have used the

Stokes preconditioned Newton method proposed by Tuckerman (1989) and Mamum & Tuckerman (1995). This technique relies on the following two main ingredients:

(i) A first order Euler time stepping code to solve the full nonlinear equations and its by product to solve the linearized equations around a basic flow. This time-stepping code is very similar in its principle to the one described in the next section. Moreover, the equations are written in stream function – vorticity function formulation.

(ii) A matrix free method, such as GMRES (Saad & Schultz 1986), to solve the linear systems involved at each Newton iteration. These matrix free methods only require computing the action of the matrix onto a vector, which amounts in our case to solving one time step of the linearized Navier–Stokes equations. This preconditioned Newton method turns out to be very efficient provided the full discrete coupled system is solved at each time step. This is achieved by using an influence matrix technique in order to enforce the no-slip condition.

3.3. Time discretization

The time evolution is computed by means of a second order time marching procedure with an implicit discretization of the linear terms and an explicit Adams-Bashforth type extrapolation of the non linear terms. This procedure is used for both full nonlinear and the linearized computations. The computation of each time step therefore amounts to the resolution of a so-called generalized Stokes problem for $(\mathbf{v}^{n+1}, p^{n+1})$, the values of the velocity and of the pressure at time $(n + 1)\Delta t$:

$$\begin{aligned} \left(\frac{3Re}{2\Delta t} \mathbf{I} - \nabla^2\right) \mathbf{v}^{n+1} + \nabla p^{n+1} &= \mathbf{S}^{n,n-1} \\ \nabla \cdot \mathbf{v}^{n+1} &= 0 \end{aligned} \quad (3.1)$$

The source terms $\mathbf{S}^{n,n-1}$ contain all the quantities which are evaluated at the previous time steps. In this time discretized problem, the velocity–pressure coupling is handled by means of an incremental projection method (Goda 1979; Daube & Le Quéré 2002).

4. Basic flow

4.1. Structure of the meridional flow

We first focus on the steady axisymmetric basic flow in the counter-rotating regime, by means of PIV measurements and numerical simulation of the axisymmetric Navier–Stokes equations.

Superimposed to the essentially azimuthal velocity field, each disk tends to impose a meridional circulation flow. The outward flow induced by the faster disk (here the top disk) recirculates at large radius towards the centre of the slower disk due to the lateral confinement. At low rotation ratio, s , the centrifugal effect of the slower disk is not strong enough to counteract the inward flow from the faster disk, and the meridional flow simply consists of a single recirculating cell, similar to that of the rotor-stator or corotating cases. On the other hand, when the rotation ratio is increased above a certain value, around 0.1 – 0.2, the slower disk induces a centrifugal flow too, and the meridional flow gets organised into a two-cell recirculating structure, separated on the slower disk by a stagnation circle where the radial component of the velocity vanishes. This property of the counter-rotating flow can be observed from the PIV measurement shown in figure 2, obtained for $s = 0.154$ and $\Gamma = 7$. The stagnation radius, around $r \approx 67 \text{ mm} \approx 0.48R$, can be distinguished near the bottom disk.

The two-cell structure of the counter-rotating flow has been first reported by Dijkstra

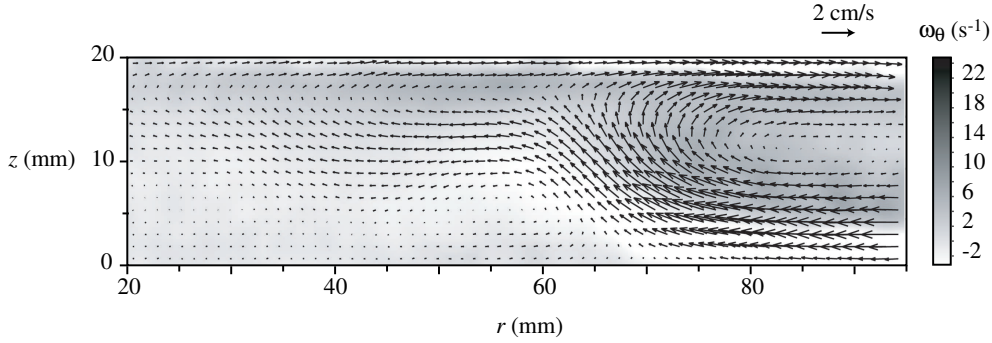


FIGURE 2. Experimental velocity field of the basic flow in the meridional plane, and azimuthal vorticity field ω_θ (grey scale), for $\Gamma = 7$, $Re_t = 130$ and $s = 0.154$. Note that only the region $0.14 \leq r/R \leq 0.68$ is shown.

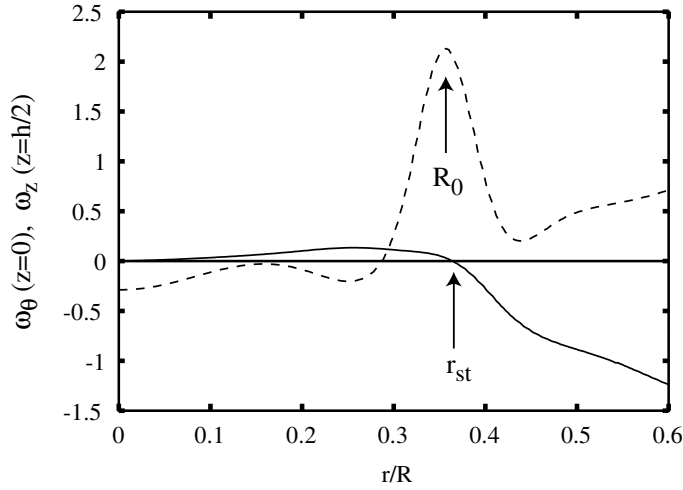


FIGURE 3. Vorticity profiles from axisymmetric simulations, illustrating the definitions of the stagnation radius, r_{st} , and the shear layer radius, R_0 . —, Azimuthal vorticity ω_θ on the bottom disk $z = 0$; --, Vertical vorticity ω_z at mid-height $z = h/2$. $\Gamma = 7$, $Re_t = 250$, $s = 0.164$ ($Re_b = 41$).

& van Heijst (1983), from axisymmetric simulation and experimental investigation at $\Gamma = 14.3$. Despite a moderate resolution, these authors clearly gave evidence of a minimum rotation ratio for the stagnation circle to appear. It has been further observed numerically by Lopez (1998) for smaller aspect ratios, $\Gamma = 2, 4$, and 8 . The importance of the two-cell structure was pointed out for the formation of the internal shear layer and its subsequent instability. Measurements at $\Gamma = 20.9$ were carried out by Gauthier *et al.* (2002) for various Reynolds numbers, and it was suspected that the stagnation circle were always present at the onset of negative spirals. However, due to uncertainty in the experimental method, no clear conclusion on the role of the stagnation circle was drawn. In order to leave this uncertainty, a systematic study of the stagnation circle has been carried out using axisymmetric stationary simulations for Γ ranging from 1 to 28 , focusing on its existence domain as function of the parameters (Γ, Re_t, s) .

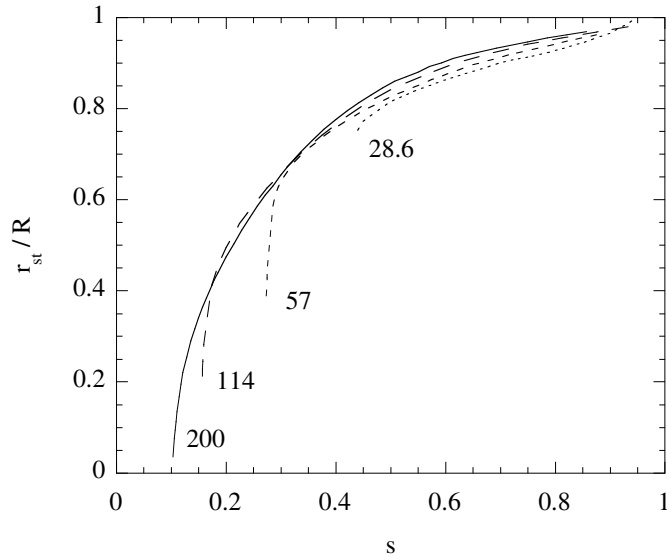


FIGURE 4. Normalized stagnation radius r_{st}/R as a function of the counter-rotation ratio $s = Re_b/Re_t$ for $\Gamma = 7$, from axisymmetric simulations. The corresponding Reynolds number of the top disk, Re_t , is indicated.

4.2. Existence domain of the stagnation circle

Figure 3 shows the azimuthal component of the vorticity, ω_θ , on the bottom disk $z = 0$ as a function of the radius. Since the velocity has zero vertical component on the disk, $\omega_\theta(z = 0)$ reduces to $\partial u_r / \partial z(z = 0)$, whose sign gives the radial velocity direction close to the disk. From this quantity the stagnation radius r_{st} is defined as the location where ω_θ crosses zero. This stagnation radius separates an inner region, $r < r_{st}$, where the flow close to the bottom disk is outward, and an outer region where the flow is inward.

Values of the normalized stagnation radius, r_{st}/R , are shown in figure 4 as a function of the rotation ratio $s = \Omega_b/\Omega_t$ for fixed values of Ω_t (the aspect ratio is kept to $\Gamma = 7$). For increasing s the growing centrifugal effect of the slower disk pushes outward the stagnation circle. In the limit of the exact counter-rotation $s \rightarrow 1$, r_{st}/R takes value close to 1, but this is not a well defined limit, since the stagnation radius is not constrained to remain on the slower disk but can rather move up to the sidewall. More important is the fact that a minimum rotation ratio, that we note s_0 , is required for the stagnation circle to appear, as first observed by Dijkstra & van Heijst (1983). In the limit of high Reynolds numbers, the different curves collapse into a single master curve, starting from $r_{st} \approx 0$ for $s = s_0 \approx 0.10$. For lower Reynolds numbers, higher values of s , around 0.2 – 0.5, are needed for the two-cell structure to develop, and the stagnation circle directly appears at a nonzero radius.

The minimum counter-rotation ratio s_0 for various aspect ratios is plotted as a function of Re_t in figure 5. These curves separate the lower part, $s < s_0$, where only one recirculating cell exists, from the upper part, $s \geq s_0$, where the two cells are present. On the same figure, experimental determinations of s_0 , obtained for $\Gamma = 20.9$ from the data of Gauthier *et al.* 2002 (see their figure 7), are also shown, and compare rather well with the present numerical results. These data have been obtained using sedimentation of small buoyant particles (Dijkstra & van Heijst 1983). The fact that the critical ratio s_0 increases as Re_t is decreased was then attributed to a possible screening effect of the

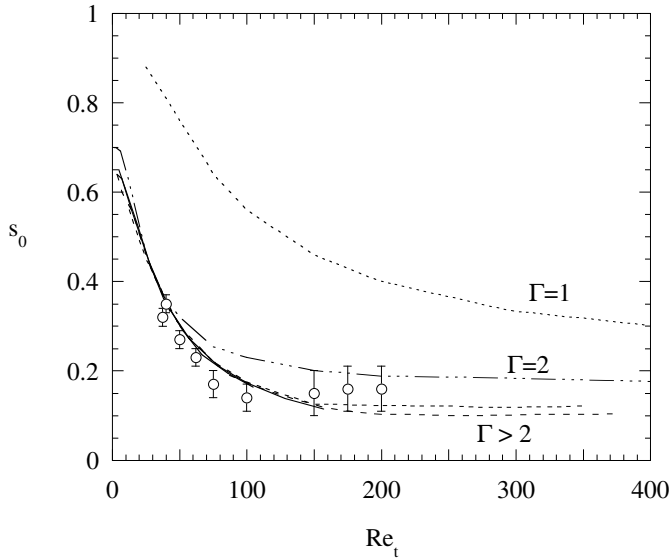


FIGURE 5. Critical counter-rotation ratio s_0 as a function of Re_t . Lines: numerical results, for various aspect ratios, $\Gamma = 1, 2, 4, 7, 14, 21$ and 28 (from up to down). \circ : Experimental measurements, for $\Gamma = 20.9$.

particles for small stagnation radius; it appears however that it is a genuine property of the meridional structure of the flow.

For sufficiently large aspect ratio, the critical ratio s_0 decreases from $s_0 \approx 0.67 \pm 0.02$ in the limit of low Reynolds numbers, and saturates towards a constant value $s_0 \approx 0.100 \pm 0.003$ for higher Reynolds numbers. It is worth pointing that the $Re_t \rightarrow 0$ limit is in excellent agreement with the computation of Dijkstra & van Heijst (1983) (see their appendix A.3), who predicted a limiting value $s_0 = 2/3$ for the Stokes flow. However, the much larger Reynolds number of their experiments and numerical simulations did not allow them to confirm this result.

The collapse of the different curves $s_0 = f(Re_t)$ for high aspect ratio, $\Gamma > 4$, is remarkable. The reason is that for a flat cavity the radius R does not play an important role in the flow structure, so that the Reynolds number $Re_t = \Omega_t h^2 / \nu$ based on the thickness h is the only relevant parameter in the problem. This similarity breaks for lower aspect ratio, around $\Gamma < 4$, for which the minimum counter-rotation ratio s_0 significantly increases, suggesting the stabilizing influence of the sidewall on the stagnation circle formation. The strong influence of the aspect ratio on the meridional structure noted by Lopez (1998) results from the fact that in his study the Reynolds number $\Omega_t R^2 / \nu = \Gamma^2 Re_t$ was kept constant as Γ was varied.

In the high aspect ratio case, the crossover between the Stokes regime, where $s_0 \rightarrow 2/3$, and the higher Reynolds number regime, where $s_0 \approx 0.10$, takes place at $Re_t \approx 60$. This Reynolds number can be expressed as $(h/\delta)^2$, where $\delta = (\nu/\Omega_t)^{1/2}$ is the lengthscale for the boundary layer thickness. The measurements of Gauthier *et al.* (2002), at $\Gamma = 20.9$, show that both the top and bottom boundary layer thicknesses, δ_t and δ_b , scale as δ , i.e. with the top (faster) disk. The top boundary layer is approximately self-similar, with a thickness given by $\delta_t/\delta \approx 2.2$. On the other hand, the bottom boundary layer shows a radial evolution, $\delta_b/\delta \approx f(r/R, s)$ for $r > r_{st}$, where the function f takes values between 2 and 4.5. These numbers allow us to give a rough estimate for the Reynolds number

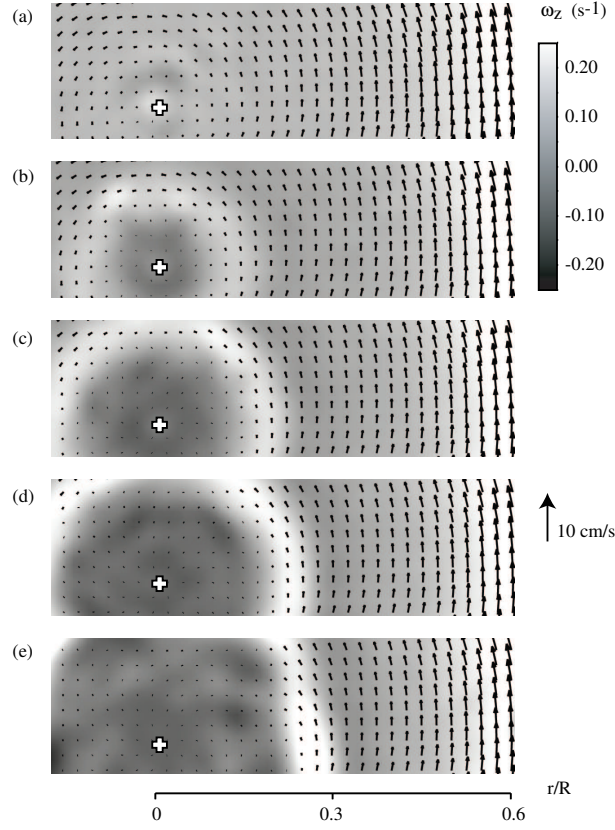


FIGURE 6. Experimental velocity fields and vertical vorticity (grey scale) at mid-height for $\Gamma = 7$, at fixed $Re_t = 289$ and increasing Re_b . (a-e): $s = 0, 0.11, 0.13, 0.15$ and 0.164 . The white cross indicates the centre of the cell. For this Re_t , the stagnation circle appears at $s_0 \approx 0.10$ (see figure 5), i.e. for the picture (b).

where boundary layer merging occurs ($\delta_t + \delta_b = h$) for all r ,

$$Re_t = \Omega_t h^2 / \nu \approx (2.2 + 4.5)^2 \approx 45. \quad (4.1)$$

Although slightly smaller, this value is of the same order as the crossover $Re_t \approx 60$ in figure 5. One may conclude that, for $Re_t > 60$, the stagnation radius results from the competition between well defined boundary layers, while for $Re_t < 60$ it results from purely viscous effects.

4.3. Structure of the azimuthal flow

In the two-cell regime, the presence of the stagnation circle has important consequence on the structure of the azimuthal axisymmetric flow, as shown in figure 6. Five velocity fields, measured at mid-height $z = h/2$, and the corresponding vertical vorticity $\omega_z = \partial u / \partial y - \partial v / \partial x$, are shown for increasing rotation ratio s , for a fixed value of Re_t . Only 1/4th of the velocity vectors are shown for clarity, but the vorticity field is computed from the entire measured velocity field. As the bottom Reynolds number is increased, an inner region of low angular velocity appears and gradually invades the outer region, in quasi-solid body rotation in the direction of the faster disk (anticlockwise). An annular shear layer, where intense vertical vorticity takes place, separates these two regions. This

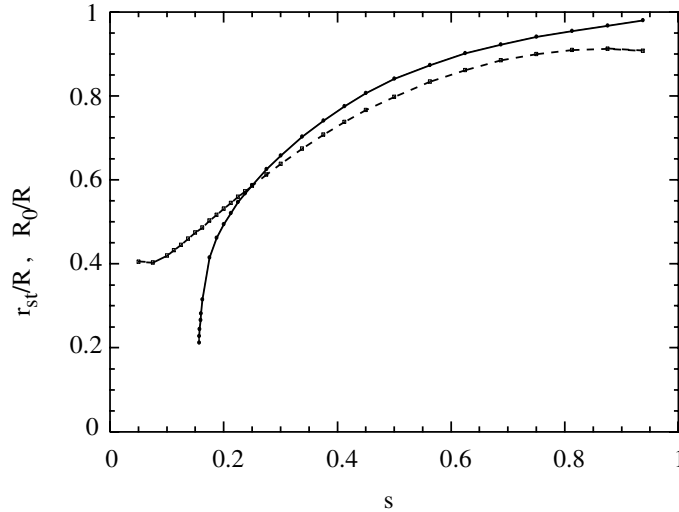


FIGURE 7. —: Stagnation radius r_{st}/R , and ---: location R_0/R of the maximum of the vertical vorticity at mid-height, as functions of the rotation ratio s . $\Gamma = 7$, $Re_t = 114$.

layer originates from the competition of the centrifugal effects of each disk, which tend to impose a constant vorticity and expell the vorticity gradient.

As shown in figure 3, the radius R_0 of the annular shear layer, defined as the location where the vertical vorticity at mid-height is maximum, approximately coincides with the stagnation radius. Measurements of R_0 as a function of s , shown in figure 7 in the case $\Gamma = 7$, confirm that this radius closely follows the stagnation radius r_{st} for $s \geq s_0$. However, this figure clearly shows that the shear layer exists for all $s > 0$, even when the stagnation circle does not exist. This means that, although the slower disk rotation may not be strong enough to develop an outward recirculation flow, it causes the inward boundary layer to decelerate, leading to a local increase of the vertical velocity. As a consequence, negative angular momentum of the slower (bottom) disk is advected upwards, leading to an annular shear layer even in the absence of a stagnation circle. But in any case, this mechanism is strongly enhanced by the presence of the stagnation circle for $s \geq s_0$, which detaches the inward boundary layer into the bulk of the flow, and an intense annular shear layer is essentially encountered when the stagnation circle is present. This annular shear layer is prone to a shear instability that breaks the axisymmetry of the basic flow as the rotation ratio s is increased, leading to the flow patterns described in the next section.

5. Instability patterns

5.1. Visualisations

When increasing the Reynolds numbers, the axisymmetric basic flow gets unstable, leading to the instability patterns that can be visualized from the light reflected from anisotropic flakes, as shown in figure 8. Here the aspect ratio $\Gamma = R/h$ ranges from 6.1 to 20.9, and the concentration of seeding flakes has been adjusted so as to keep an acceptable contrast.

The instability patterns basically consist of a sharp-cornered polygon of m sides, surrounded by a set of $2m$ outer spiral arms. For instance, one can clearly see in figure 8(b) the $m = 4$ -sided polygon together with the $2m = 8$ outer spiral arms. In addition a set

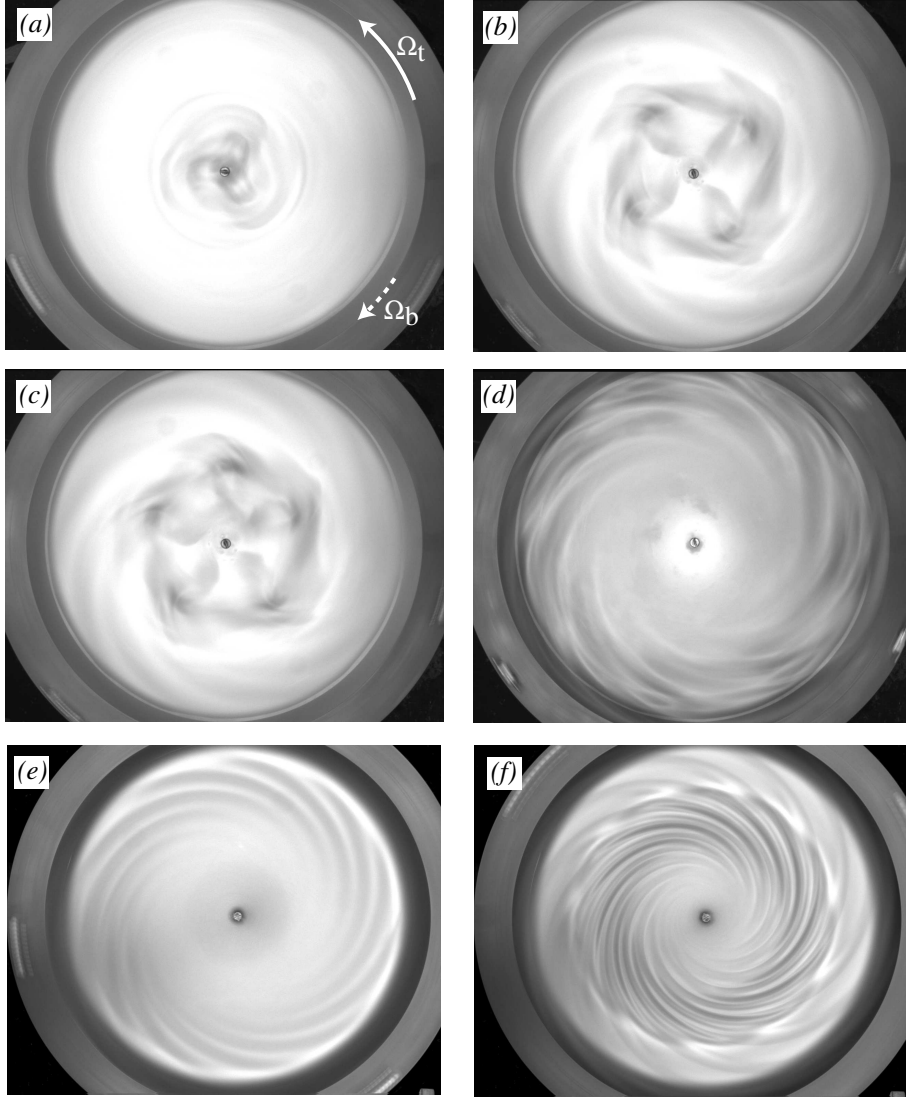


FIGURE 8. Instability patterns visualised by seeding flakes. (a) $(\Gamma, Re_t, Re_b) = (6.1, 584, 79)$, showing a mode $m = 3$. (b) $(7, 282, 47.1)$, $m = 4$. (c) $(7, 282, 51.8)$, $m = 5$. (d) $(10.8, 60.6, 26.8)$, $m = 7$. (e) $(20.9, 46, 10.5)$, $m = 11$. (f) $(20.9, 74, 13.6)$, $m = 11$. The flow is only visible on a central circle, $r \leq 0.83R$, due to the shadow from the cylindrical rim. Disks rotation are indicated by the arrows in picture (a).

of m inner arms connecting the corners of the polygon to the centre also appears, which turns to spiral arms too as the aspect ratio Γ is increased. Close to the onset, the pattern slowly rotates as a whole, at an angular velocity intermediate between the velocities of the two disks.

Depending on the mode and the aspect ratio, only the polygon or the inner spiral arms may be observed. Low aspect ratios and/or low modes essentially leads to the polygon pattern (figure 8a–c, with $m = 3, 4$ and 5), similar to those observed by Lopez *et al.* (2002) at $\Gamma = 2$ using dye visualization. Higher aspect ratios and/or higher modes mostly show the inner spiral arms (figure 8d–f, with $m = 7$ and 11). Both the m inner

arms and the $2m$ outer arms can be seen in figure 8(*f*), and the corners of the polygon appears as bright V-shaped patterns where the m arms split into $2m$ arms. On the other hand only the m inner spiral arms can be seen in figure 8(*e*). In this figure the polygon and the outer spiral arms extend to larger radii, where visualization are not possible due to the cylindrical rim.

The spiral arms seen here correspond to the *negative* spirals described by Gauthier *et al.* (2002), where the observations were restricted to $\Gamma = 20.9$. The name of *negative* spirals has been chosen because they roll up to the center in the direction of the slower disk – but also to distinguish them from the *positive* spirals, another pattern that arises from a boundary layer instability in the inward layer close to the slower disk, and which is also present in the rotor-stator and corotating flows.

As the Reynolds numbers are increased slightly beyond their transition values, higher order modes quickly superimpose on the fundamental one, eventually leading to a disordered pattern. In this study we are only interested in the onset patterns, and the Reynolds numbers are kept in the close vicinity of the onset of the instability.

The relationship between the light intensity reflected by the flakes and the velocity gradient tensor field of the flow is non trivial in the general case (Savas 1985; Gauthier *et al.* 1998). Although the intensity field may represent the depth-averaged orientation of the flakes, at least in low seeding regime, screening effects from the upper regions may considerably alter the interpretation of the observed patterns, so that the flow structure can not be directly inferred from the visualizations of figure 8. This visualisation method is nevertheless convenient for a first approach, as it allows us to easily define the domains of parameters of interest where more quantitative measurements should be performed.

5.2. Onset curves

The experimental onset curves of the patterns is shown in figure 9 in the plane of parameters (Re_t, Re_b) for various aspect ratios Γ ranging between 2 and 20.9. These curves are obtained by slowly increasing the bottom disk angular velocity Ω_b at fixed value of Ω_t and visually inspecting the intensity pattern of the light reflected by the flakes. No hysteresis is observed within our experimental uncertainty, of around 3%. The scatter mainly originates from the very large growth time of the instability close to the onset, which can be as large as 10 to 100 rotation periods of the faster disk. For high aspect ratio, boundary layer instabilities arise at moderate Reynolds numbers, and the onset curves for the shear layer instability become defined for a narrow range of Re_t . It is worth pointing out that, although no hysteresis is observed for the instability threshold, noticeable hysteresis is present for the onset mode, that will be described in section 6.2. The point $(\Gamma, Re_t, Re_b) = (2, 250, 102)$ obtained by Lopez *et al.* (2002), also shown in figure 9, is in excellent agreement with the present results.

In the same figure the border lines separating the one-cell and two-cell domains are also plotted. In the plane (Re_t, Re_b) , these lines are given by $Re_b = s_0 Re_t$, where $s_0(\Gamma, Re_t)$ is the minimum rotation ratio for the two-cell structure and the associated stagnation circle to appear, introduced in section 4.2 (see figure 5). From this figure it appears that the stability curves essentially fall into the two-cell domain, except for the highest aspect ratio, around $\Gamma > 16$, for which the instability arises in the upper part of the one-cell domain. It is worth noting that, for low aspect ratios, the presence of the two-cell structure is not a sufficient condition for the basic flow to get unstable, and a much higher Re_b is needed for the instability to arise.

Figure 10 shows the same data as in figure 9, but plotted in the plane of parameters $(\Gamma Re_t, \Gamma Re_b)$. Using this new set of parameters, the different onset curves appear to collapse approximately into a single master curve, except for the one corresponding to

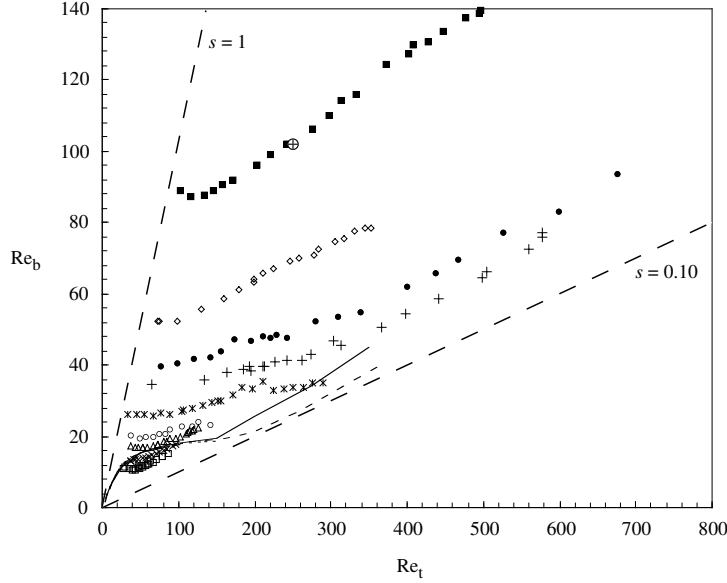


FIGURE 9. Stability curves for various aspect ratios $\Gamma = R/h$ from 2 to 21. ■: $\Gamma = 2$. ◇: 3. ●: 5.2. +: 7. *: 9.3. ○: 12.6. △: 14.4. ×: 18. □: 20.9. ⊕: Instability threshold obtained by Lopez *et al.* (2002), at $\Gamma = 2$. The curves indicate the stagnation circle onset (same line patterns as in figure 5), and separate the one-cell domain (lower region) from the two-cell domain (upper region). The long dashed lines indicate the exact counter-rotation slope, $s = 1$, and the slope $s = s_0 \simeq 0.10$ corresponding to the critical rotation ratio for the two-cell structure at high Reynolds number.

the lowest aspect ratios, $\Gamma = 2$ and 3, which slightly depart from it. The fact that the polygon pattern and the negative spirals share the same onset curve indicates that they both arise from the same instability mechanism, although the nonlinear saturation leads to very a different morphology. The bunch of curves start from $\Gamma Re_b \approx 200 \pm 40$ and gather towards a constant rotation ratio line, $s \approx 0.13 \pm 0.01$, slightly beyond the rotation ratio for the onset of the two-cell structure, which that takes place at $s_0 \approx 0.10$ for high Reynolds numbers.

The collapse of the stability curves observed in figure 10 gives first indication that the mechanism responsible for this instability is a shear layer instability, because the shear and the boundary layers behave differently as Γ is varied. At given disks velocities, increasing the gap h decreases the shear strength but does not affect the boundary layers thickness, which are governed by the faster (top) disk velocity, $\delta \sim (\nu/\Omega_t)^{1/2}$. If the observed patterns would have arise from a boundary layer instability mechanism, then the relevant control parameters should have been the Reynolds numbers based on the radius of the cell $\Gamma^2 Re = \Omega^2 R^2/\nu$. Indeed the characteristic velocity in the boundary layer of thickness δ is of order of $\sim \Omega R$, so that this instability should be controlled by the Reynolds number $\sim \Omega R \delta/\nu \sim (\Gamma^2 Re_t)^{1/2}$. By contrast, if we now assume that the growth rate is controlled by the global shear $\gamma \sim \Omega R/h$, damped by viscous diffusion on a timescale $\tau_v \sim h^2/\nu$, then the natural control parameter is $\gamma \tau_v = \Omega R h/\nu = \Gamma Re$. This is actually a rough estimate, since the instability takes place for radii that may be much lower than the cell radius R . But still the collapse of the curves when rescaled as $(\Gamma Re_t, \Gamma Re_b)$, in figure 10, indicates that a shear layer instability mechanism is indeed responsible for the observed patterns. This mechanism will be confirmed in section 6.1, where a local analysis of the shear layer is presented.

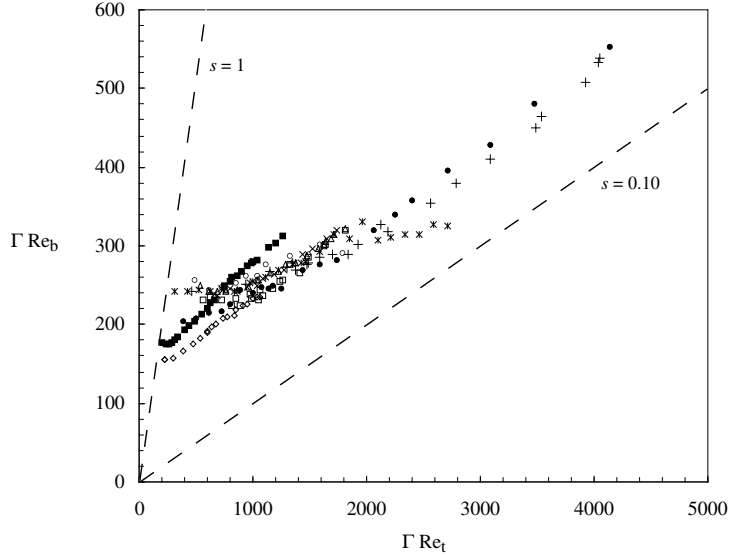


FIGURE 10. Stability curves. Same data as in figure 9, but plotted in the $(\Gamma Re_t, \Gamma Re_b)$ plane of parameters. The basic axisymmetric flow is stable in the lower region.

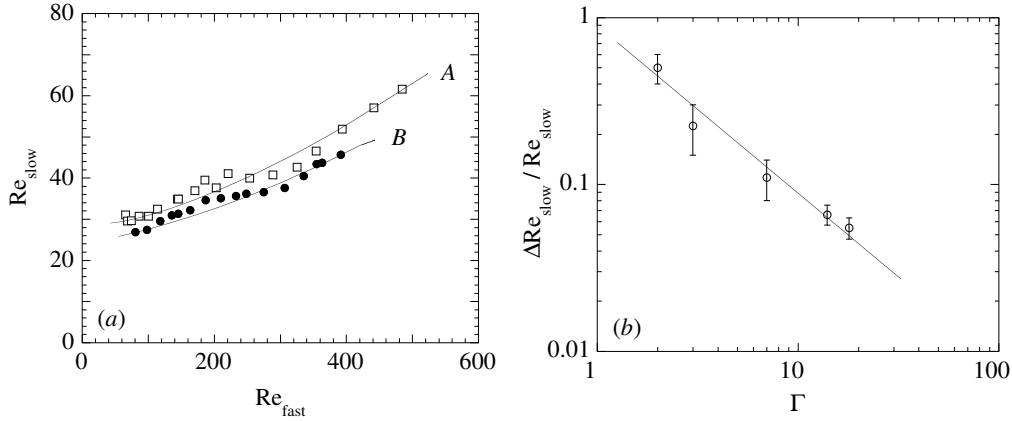


FIGURE 11. (a) Stability curves for an aspect ratio $\Gamma = 7.2$. \square , Configuration A: the sidewall rotates with the faster disk; \bullet , Configuration B: the sidewall rotates with the slower disk. (b) Relative deviation of the threshold between configurations A and B as a function of Γ . The line shows $0.9\Gamma^{-1}$.

Influence of the rotating sidewall

As the sidewall rotates with one of the two disks, the flow configuration is not invariant by reflection with respect to the horizontal plane. The influence of the sidewall is expected to be negligible in the limit of large aspect ratio Γ , but may be significant for the range of Γ spanned in the present study. It may be therefore of interest to compare the stability curve of the actual flow configuration with the one of the symmetric configuration. We call here *configuration A* (resp. *B*) the situation where the sidewall rotates with the faster (resp. slower) disk. We introduce $(Re_{\text{fast}}, Re_{\text{slow}})$ the Reynolds numbers based respectively on the faster and slower rotating disk; it is given by (Re_t, Re_b) in configuration A and (Re_b, Re_t) in configuration B. Experimentally, configurations A and B are simply obtained by exchanging the angular velocities Ω_t and Ω_b .

Figure 11(a) shows the stability curve in configurations A and B for an aspect ratio $\Gamma = 7.2$ in the plane of parameters $(Re_{\text{fast}}, Re_{\text{slow}})$. The thresholds in configuration B appear to be around 11% lower than that of configuration A , with no significant trend as the Reynolds number is varied. In configuration A , the fluid rotation due to the faster disk is sustained by the corotating sidewall, and the resulting flow at the periphery of the cell is closer to a solid body rotation. As a result, the stagnation circle where the centrifugal effects of each disk balance is smaller, and the internal shear layer is weakened, so that configuration A is more stable than B . Furthermore, boundary layer instabilities (where the stability curves end) occur at a lower Reynolds number in the configuration B than in A . These instabilities originate from the deceleration of the inward boundary layer over the slower rotating disk. In configuration B , since the slower disk rotates together with the , the deceleration effect is stronger and the inward boundary layer is more unstable.

If we expect the boundary condition at $r = R$ to have an influence of order of h/R on the rest of the flow, then the relative deviation between the thresholds of configurations A and B should decrease as Γ^{-1} . This is indeed the case, as shown in figure 11(b), where the normalized threshold difference $\Delta Re_{\text{slow}}/Re_{\text{slow}}$ is plotted as a function of the aspect ratio, with $\Delta Re_{\text{slow}} = Re_{\text{slow},A} - Re_{\text{slow},B}$. The inverse law fit gives $\Delta Re_{\text{slow}}/Re_{\text{slow}} \approx 0.9\Gamma^{-1}$, and the error bars reflect the variability of the deviation along the curves in figure 11(a). The difference between the configurations A and B remains small for high aspect ratio, as far as the instability threshold of the counter-rotating flow is concerned, and in the following we will restrict ourselves to the configuration A .

5.3. Numerical and experimental description of the flow patterns

In order to get further insight into the instability mechanism of the counter-rotating flow, PIV measurements and numerical simulations have been performed in the close vicinity of the onset curves.

Figure 12 shows the horizontal velocity field and the associated vertical vorticity field, measured by PIV at mid-height, $z = h/2$, for $\Gamma = 7$. As previously, only 1/4th of the velocity vectors are shown, and the vorticity colour map has been rescaled so that to display the same flow characteristics in each case. Figure 12(a) shows the axisymmetric basic flow, while the three bifurcated fields in figures b,c and d , show azimuthal modulations of modes $m = 5, 4$ and 3 , obtained for increasing (Re_t, Re_b) along the onset curves.

The annular shear layer is found to evolve towards a sharp-cornered polygonal pattern, each side containing a local minimum and maximum of vorticity. The modulation of the vorticity level along the shear layer is similar to the classical Kelvin-Helmholtz ‘cat’s eyes’ pattern for the linear case. The vorticity maxima are located slightly downstream the corners of the polygon, which probably results from a nonlinear deformation of an initially periodic chain of vorticity extrema. The $2m$ surrounding spiral arms present in the visualizations in figure 8 can not be seen here, indicating that they are not located in the mid-height plane.

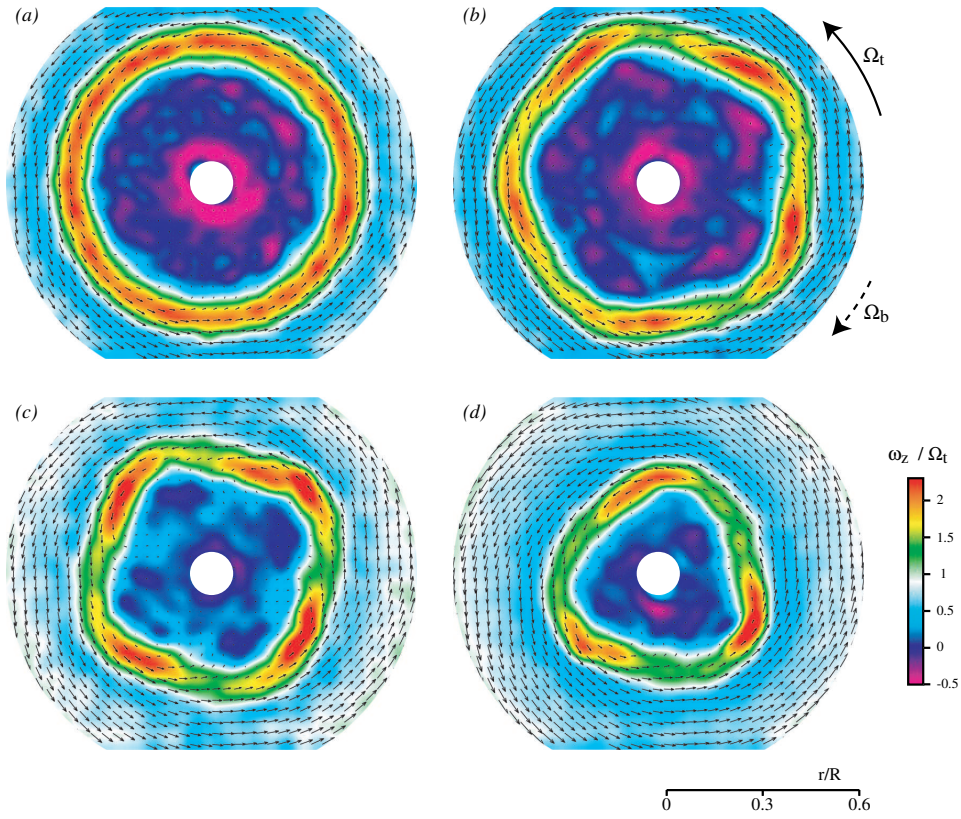


FIGURE 12. Experimental velocity and vorticity fields ω_z at mid-height $\Gamma = 7$. The first picture is below the onset, and the three following ones are for increasing Reynolds numbers along the onset curve. (a), $(Re_t, Re_b) = (240, 40)$; (b), $(240, 43)$; (c), $(289, 45)$; (d), $(341, 50)$.

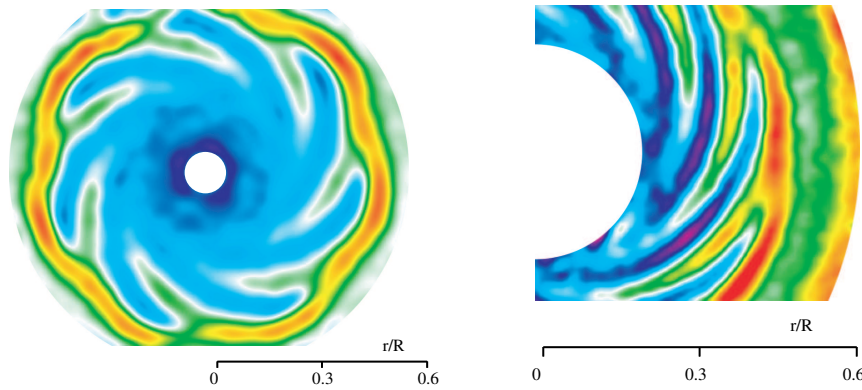


FIGURE 13. Experimental vorticity fields ω_z at mid-height. (a), $(\Gamma, Re_t, Re_b) = (9.3, 183, 28.5)$, mode $m = 7$. (b), $(14, 80, 19)$, mode $m = 8$. The colour maps are the same as in figure 12.

[COLOR PLATE 1]

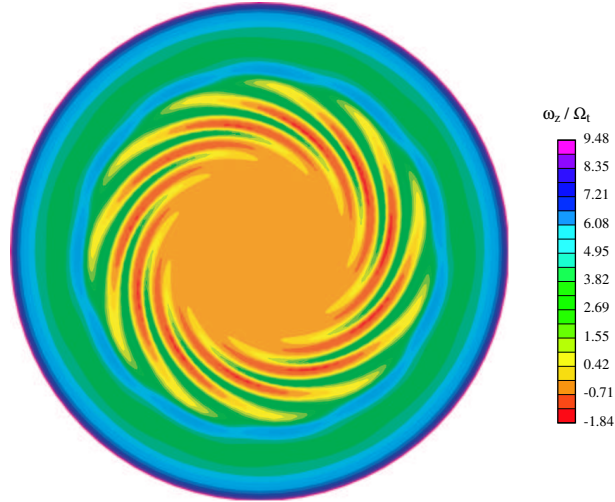


FIGURE 14. Numerical vorticity field ω_z at mid-height $z = h/2$ for $\Gamma = 21$, $Re_t = 67$, $Re_b = 14.3$, showing a mode $m = 11$. Only the central circle $r \leq 0.95R$ is shown.

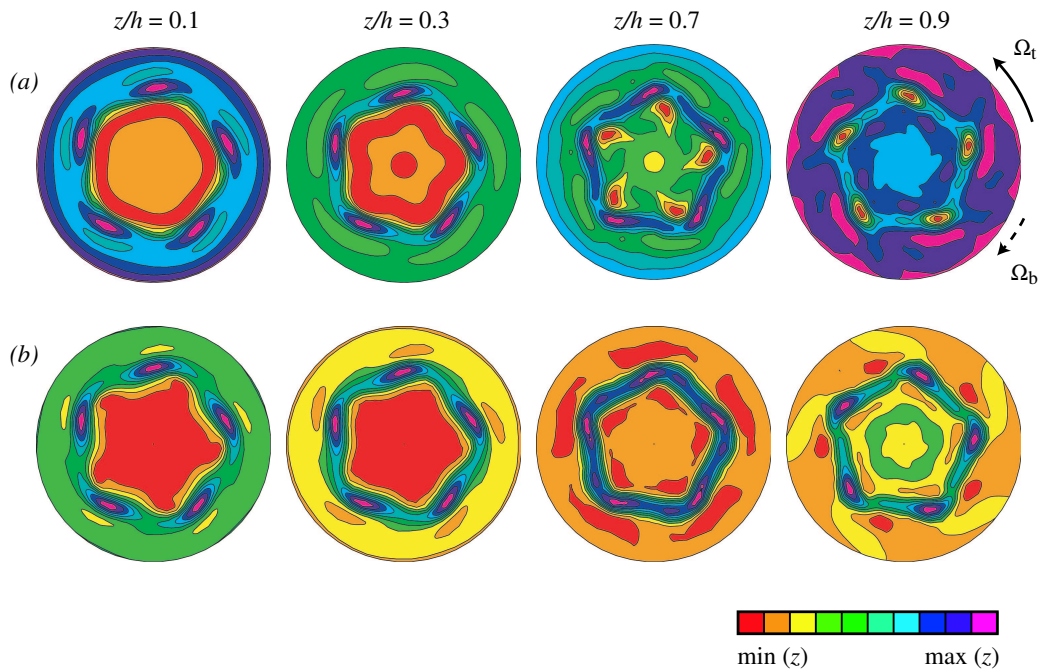


FIGURE 15. Numerical axial vorticity ω_z (a) and axial velocity v_z (b) at different heights $z/h = 0.1$ (close to the slower disk), 0.3, 0.7 and 0.9 (close to the faster disk), for $\Gamma = 7$, $Re_t = 250$, $Re_b = 57$, showing a mode $m = 5$. The colour maps for both ω_z and v_z are normalized by their minimum and maximum on each field. Only the central circle $r/R \leq 0.6$ is shown.

[COLOR PLATE 2]

The case of flatter cavities is illustrated in figures 13(a), for $\Gamma = 9.3$, and 13(b), for $\Gamma = 14$. The same modulated shear layer can still be seen, but the vertical confinement leads to a saturated pattern that gets more complex than the one observed for low Γ . In addition to the polygonal shear layer, a set of m spiral arms appears in the centre of the flow, where local vorticity minima, of the same sign of the slower rotating disk, gets concentrated. Following the definition introduced by Gauthier *et al.* (2002), these spiral arms are *negative*: they roll up to the centre in the direction of the slower disk.

Because of the above mentioned limitations in the PIV measurements, the structure of the vorticity field for even flatter cavities can only be investigated from the numerical simulations. The case $\Gamma = 21$, illustrated in figure 14, where the same characteristic features can be seen, shows a thinner shear layer which leads to a higher order mode, here $m = 11$. Only the inner m spiral arms can be seen: here again, the $2m$ outer spiral arms take place out of this slice, $z = h/2$. The similitude with the visualisation in figure 8(e) is remarkable.

The three-dimensional structure of the pattern can be inferred from the numerical vorticity and vertical velocity fields shown in figure 15 for $\Gamma = 7$, for heights z ranging from $0.1h$ (close to the slower disk) up to $0.9h$ (close to the faster disk). From these figures, one can see the vertical structure of the polygonal shear layer, and the influence of the boundary layers of each disk.

It is remarkable that the location of the vorticity extrema approximately coincide on each field, suggesting that the flow structure is roughly invariant along the vertical direction, except close to the disks where boundary layers take place. Along these columnar vortices strong upward flow is present, which advects negative vorticity from the bottom to the top disk. Close to the faster disk (4th slice), the outer spiral arms appear surrounding the polygonal shear layer. Slight vorticity modulations show $2m$ extrema along the azimuthal direction, similar to the $2m$ outer spiral arms seen in figure 8(c). These spiral arms result from the interaction of the shear layer primary instability pattern in the bulk of the flow with the centrifugal Ekman boundary layer over the faster disk. The Ekman layer advects the perturbation outwards with an anticlockwise rotation, resulting in the observed negative spirals. Since they are essentially localized near the top disk, these negative spirals clearly appear from the seeding flakes visualizations in figure 8, although they are associated with very weak vorticity modulation.

5.4. Growth rates and nonlinear saturation of the instability

Experimental results

We now investigate experimentally the growth rates and the nonlinear saturation of the bifurcated flow slightly above the onset. The energy of the instability pattern may be defined as the difference between the total energy of the flow and the energy of the unstable axisymmetric basic flow. Since the unstable basic flow can obviously not be deduced from experimental measurements of the bifurcated flow, we approximate it by the azimuthal average of the total energy. Note that we are only dealing with the contribution of the horizontal components of the velocity at a given height, since the vertical component is not accessible from our two-dimensional PIV measurements.

Within these approximations, the energy per unit mass of the bifurcated flow at a given height can be written

$$\Delta E = \frac{1}{2} \frac{1}{\pi R^2} \int_0^{2\pi} \int_0^R \left\{ [v_r(r, \theta) - \bar{v}_r(r)]^2 + [v_\theta(r, \theta) - \bar{v}_\theta(r)]^2 \right\} r \, dr \, d\theta, \quad (5.1)$$

where the overbars denote the azimuthal average of the horizontal components of the instantaneous velocity field. Since the bifurcated state is very sensitive to the distance

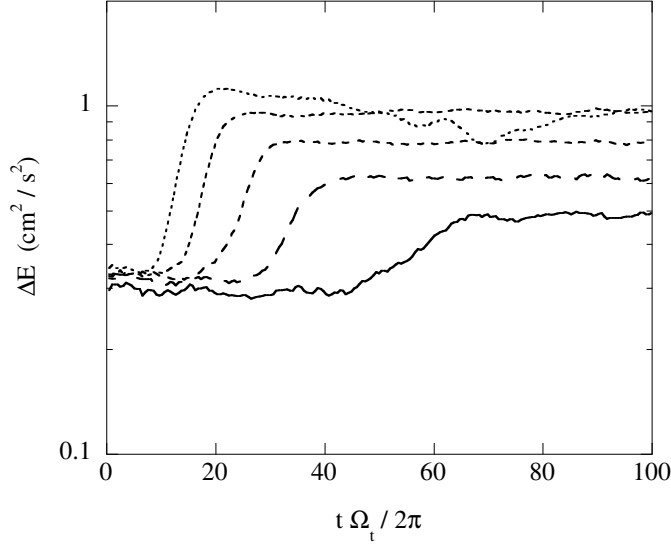


FIGURE 16. Energy of the non axisymmetric part of the flow, equation (5.1), as function of time, after a sudden increase of Re_b at $t = 0$ s from 70 to 75, 76, 77, 78 and 79 (from solid line to short dashed line), computed from the velocity fields of figure 17 ($\Gamma = 3$ and $Re_t = 280$).

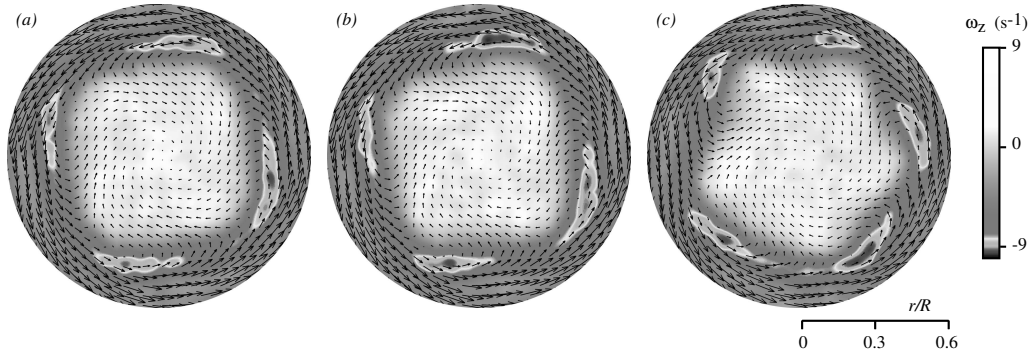


FIGURE 17. Experimental velocity and vorticity fields for $\Gamma = 3$ and $Re_t = 280$. (a), $Re_b = 75$; (b), $Re_b = 77$; (c), $Re_b = 79$.

to the threshold, the PIV measurements have been performed at small aspect ratio, $\Gamma = 3$, where a wider range of Reynolds numbers can be explored before secondary instabilities occur. For this aspect ratio the pattern is confined to small radii, and the radial integration in the equation (5.1) has been restricted to the range $0 \leq r \leq 0.64R$.

Figure 16 shows the energy ΔE as a function of time for a fixed value $Re_t = 280$, after a sudden increase of Re_b at $t \approx 0$, from a value slightly below the threshold, 70, up to values between 75 and 79. The corresponding flow patterns are shown in figure 17, where the grey scale has been chosen in order to emphasize the local vorticity extrema of the shear layer.

At $t = 0$, the flow is purely axisymmetric, and the nonzero value of ΔE simply corresponds to the noise level of the PIV measurements and the azimuthal average procedure. For $Re_b \in [75, 78]$, after a transient growth, the energy saturates towards a constant value, which is an increasing function of Re_b . The growth rate also appears to be an

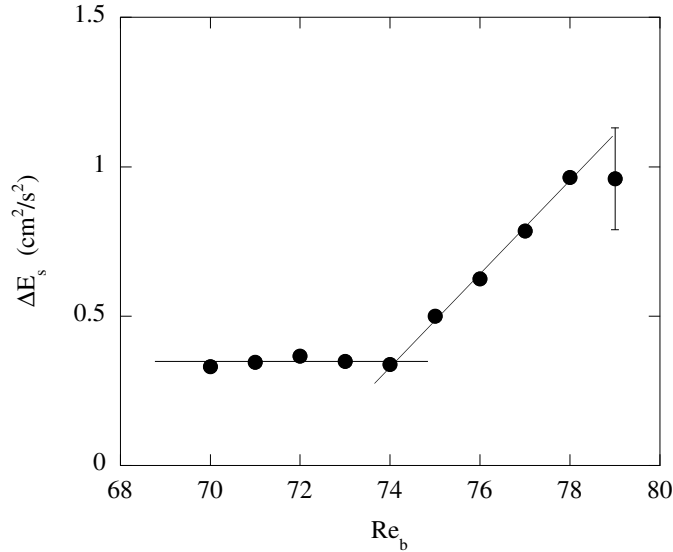


FIGURE 18. Energy of saturation of the bifurcated state, equation (5.1), as a function of Re_b ($\Gamma = 3$, $Re_t = 280$).

increasing function of Re_b . For $Re_b = 79$, the pattern is a combination of modes $m = 4$ and 5 (figure 17c), and ΔE does not show saturation.

The level of saturation of the energy, ΔE_s , is plotted in figure 18 as a function of Re_b . For $Re_b \leq 74$, the energy of the stable axisymmetric flow is constant and equal to the noise level, and above the instability threshold, $Re_{b,c} \approx 74$ here, the energy linearly increases as $Re_b - Re_{b,c}$, as expected for a supercritical bifurcation. At $Re_b = 79$ the error bar reflects the oscillations associated to the mixed state $m = 4$ and 5.

These results compare well with the findings of Gauthier *et al.* (2002), who observed in the case $\Gamma = 20.9$ that the time of appearance of the spirals increased linearly as $Re_b - Re_{b,c}$ above the transition (see their figure 17). This time of appearance was determined by visual inspection of the intensity pattern of the reflected light, and is believed to give an estimate of the growth time of the instability. The present method provides another signature of a supercritical bifurcation, and we believe that the bifurcation remains supercritical for all the range of aspect ratio spanned in this paper.

Linear computations

Linear numerical computations have been performed for the same flow parameters, $\Gamma = 3$ and $Re_t = 280$, in order to provide further insight into the observed modes. From the modal energies, shown in figure 19 below and above the transition, the growth rate σ of each mode can be computed from the exponential growth regime (note that the modal energies now correspond to the true three-dimensional energy over the whole flow). They are plotted in figure 20 as functions of Re_b . The most unstable mode is $m = 3$ at $Re_b = 72.3$, but it is closely followed by the mode $m = 4$, that becomes more unstable for $Re_b > 73.9$. This mode $m = 3$ was not observed experimentally, probably due to our limited resolution on the Reynolds numbers, of order of 3%. If Re_b is further increased, the dominant mode becomes $m = 5$, for $Re_b = 78.9$, which is in excellent agreement with the experiment (figure 17).

It must be noted that the experimental apparent growth rates, which can be estimated from figure 16, take values that are significantly smaller than the numerical ones: $\sigma \simeq$

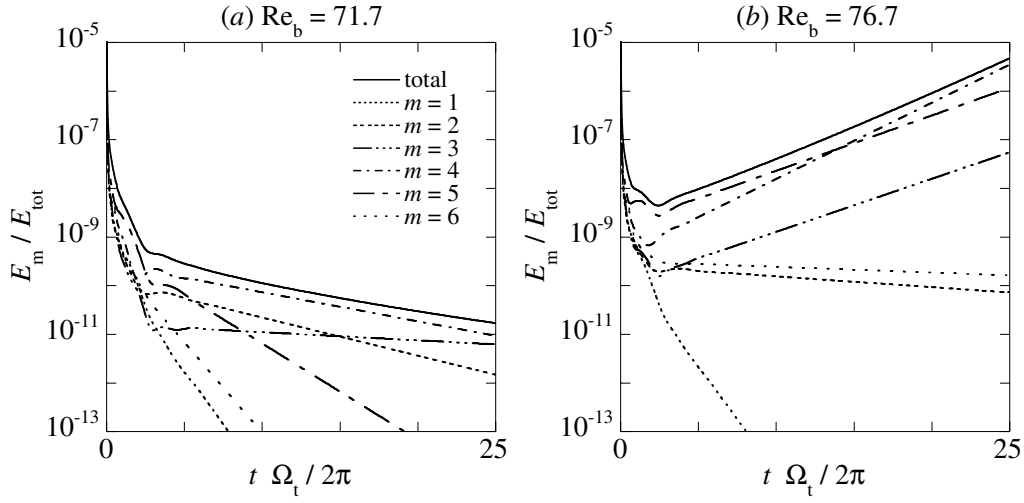


FIGURE 19. Normalized energy for the modes $m = 1 - 6$ (dashed lines) and total energy of the perturbation (solid line), as a function of time normalized by the rotation period of the faster disk, for $\Gamma = 3$ and $Re_t = 280$. (a), $Re_b = 71.7$. (b) $Re_b = 76.7$.

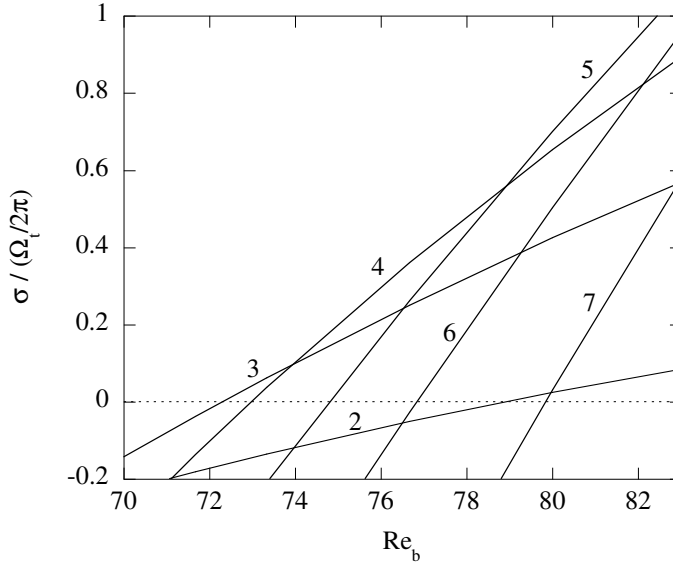


FIGURE 20. Non dimensional growth rate of the different modes as a function of Re_b , for $\Gamma = 3$, $Re_t = 280$.

$(0.013 \pm 0.005)\Omega_t/2\pi$ for $Re_b = 75$, up to $\sigma \simeq (0.10 \pm 0.015)\Omega_t/2\pi$ for $Re_b = 79$, i.e. about 5 times smaller than the numerical growth rates of figure 20. This discrepancy probably originates from the fact that only the very late time before the nonlinear saturation can be measured experimentally, and the earlier exponential growth falls largely below the experimental noise level.

The numerically observed modes for $\Gamma = 3$ are summarized in the marginal stability curve in figure 21(a). The modes obtained experimentally at $\Gamma = 3$ are also shown for comparison. Figure 21(b) shows similar results for $\Gamma = 7$, for the same value $Re_t = 280$. In both cases the critical mode is $m = 3$. These curves emphasize the important sensitivity

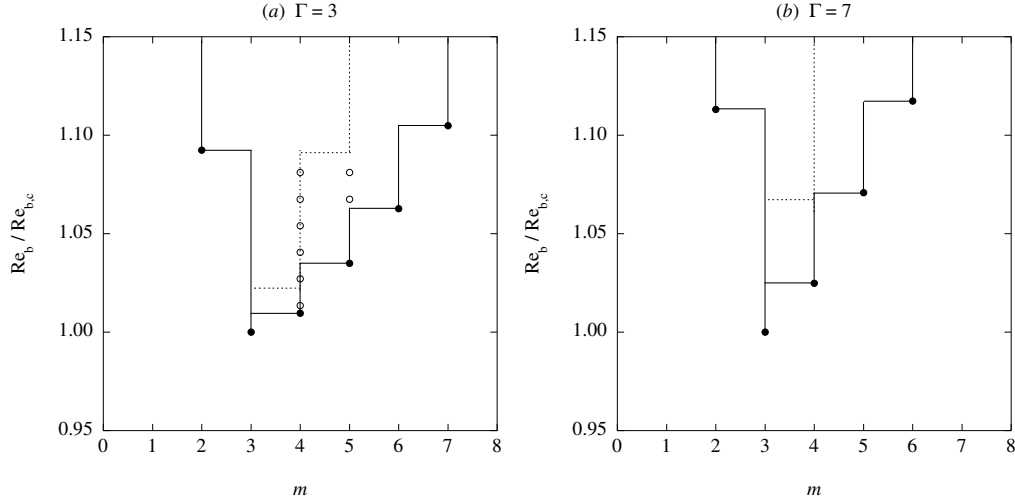


FIGURE 21. Marginal stability curves and most unstable mode (---), obtained from the linear computations for $Re_t = 280$, as a function of $Re_b/Re_{b,c}$. •, critical Reynolds number for a given mode m . The lines joining the points are guide for the eyes. (a) $\Gamma = 3$, $Re_{b,c} = 72.3$; ○, experimentally observed modes. (b) $\Gamma = 7$, $Re_{b,c} = 37.8$.

of the onset mode slightly beyond the instability threshold, with step heights of the order of 3%. This sensitivity seems to slightly decrease as the aspect ratio Γ is increased, at least when $Re_t =$ is kept constant. In any case it remains of the order of the experimental uncertainty, around 3%, making difficult any accurate determination of the onset mode.

Nonlinear computations

Since in the experiment the Reynolds number cannot be kept in the close vicinity of the transition, one may expect nonlinearities to significantly affect the selected modes. In order to check this point, nonlinear numerical computations have been performed at $\Gamma = 3$, $Re_t = 280$ and $Re_b = 80$, i.e. 11% beyond the transition. For these values, linear computations show that the modes $m = 2$ to 7 are unstable, the most unstable being the mode $m = 5$ (see figure 20).

Figure 22 shows the long-time evolution of two different computations performed for the same flow parameters, which differ only by the initial condition. The axisymmetric stable flow for $Re_b = 70$ is taken as the initial condition for the first computation (figure 22a), in a similar way as for the experiments, where Re_b was suddenly increased from 70 to a value above the threshold. For the second computation (figure 22b), the bottom Reynolds number has been gradually increased from 70 up to 80 in four steps, waiting for the saturation of the flow at each step (typically 300 rotation periods of the faster disk).

While the first computation (a) shows a mode $m = 5$, the second one (b) shows a mode $m = 4$. For similar values of Re_b (see figure 17c), the experiment shows a mixed state, dominated by the modes 4 and 5. The progressive increase of Re_b in the second case probably constrained the flow to follow the metastable branch $m = 4$, although other branches may be more unstable. These observations clearly illustrate the sensitivity of the observed pattern to the initial condition. They are in good agreement with a number of experimental observations, where strong hysteresis is observed for the modes, although no hysteresis is present for the value of the threshold. This situation is generic for systems

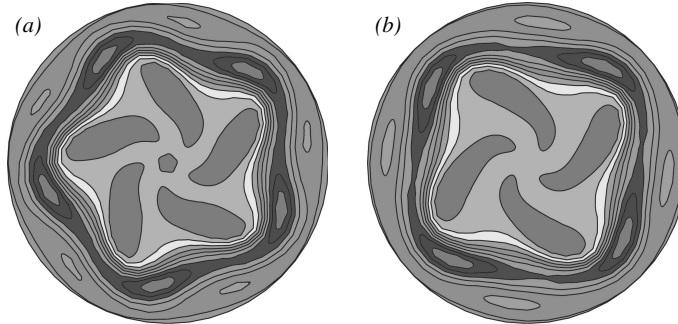


FIGURE 22. Iso-vorticity levels at mid-height obtained for the same parameters, $\Gamma = 3$, $Re_t = 280$, $Re_b = 80$, starting from different initial conditions. (a), from sudden increase of Re_b from 70, showing a mode $m = 5$. (b), from progressive increase of Re_b from 70, showing a mode $m = 4$. Only the central circle $r \leq 0.65R$ is shown.

where the geometrical confinement leads to azimuthal wavenumber quantization (see, e.g., Rabaud & Couder 1983).

6. Characterisation of the shear layer instability

6.1. Local control parameter for the shear layer instability

The experimental and numerical vorticity fields in figures 12–15 and the collapse of the onset curves in figure 10 strongly suggest that the basic mechanism responsible for the observed flow pattern is a shear layer instability. A natural way to assess this point is to compute the local Reynolds number based on the thickness w of the shear layer and the velocity jump ΔU across it,

$$Re_\delta = \Delta U w / \nu. \quad (6.1)$$

It is expected that, just below the onset of the instability, this local Reynolds number reaches a unique critical value.

A series of PIV measurement for $\Gamma = 7$ along the onset curve has been performed, and the shear layer thickness and velocity difference have been extracted from the velocity fields. Figure 23 shows two azimuthal velocity profiles, averaged over $[0, \pi]$ (negative r correspond to the other half $[\pi, 2\pi]$). They correspond to two different top Reynolds numbers but, in each case, the bottom Reynolds number has been set just below its corresponding critical value. Both profiles consist of two pieces of quasi-solid body rotation separated by a rather sharp velocity front, as already noted in figure 6. The inner region rotates here in the direction of the slower disk, with an angular velocity of about $-0.5\Omega_b$, while the outer region rotates with the faster disk, at $\sim 0.3\Omega_t$. While the former value probably strongly depends on the height z , it is interesting to note that the latter value is close to the angular velocity found in the inviscid core of the Batchelor (1951) flow, $v_\theta(r) \approx 0.313\Omega_t r$ (see Zandbergen & Dijkstra 1987). The angular velocity increases for $r > 75$ mm, and eventually reaches Ω_t for $r = R$.

From this figure the velocity jump ΔU is computed as the difference between the surrounding extrema across the front, and the thickness w as the distance between these extrema. Only the horizontal projection of the thickness is actually measured. However, since the shear layer was shown to be almost vertical (see the numerical vorticity fields in figure 15), at least for moderate Γ , the apparent thickness gives a reasonable estimate of the actual one. This thickness is found to be of order of the gap between the disks, $w \approx (0.6 \pm 0.1)h$, and shows no significant variation with the Reynolds number. The

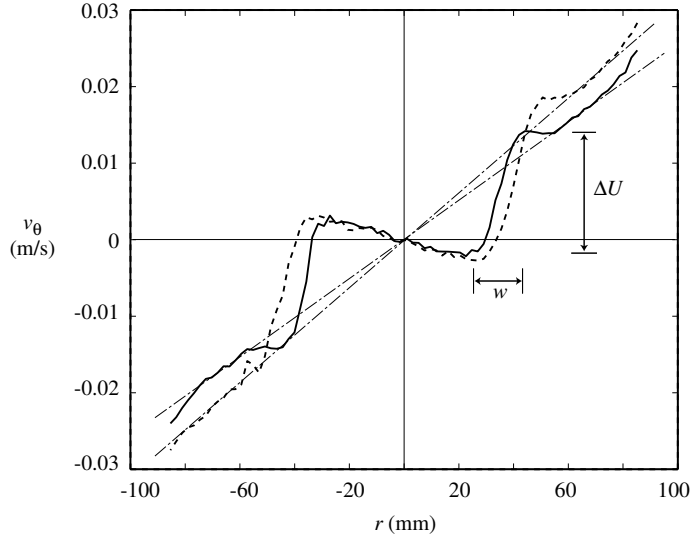


FIGURE 23. Azimuthal velocity profiles $v_\theta(r)$ computed from PIV fields at mid-height $z = h/2$, measured just below the onset of instability, for $\Gamma = 7$. $---$, $Re_t = 239$; $—$, $Re_t = 277$. The corresponding solid-body rotation profiles $v_\theta(r) = 0.3\Omega_t r$ are also shown for both Re_t ($---$). Only the central circle $r \leq 0.6R$ is measured. The definitions of the shear layer thickness w and velocity jump ΔU are sketched for the curve $—$.

scaling $w \propto h$, although not tested experimentally for other aspect ratios, is in qualitative agreement with experimental and numerical fields (see figures 13 and 14), from which the shear layer thickness appears to decrease as Γ is increased.

The local Reynolds number computed from these measurements is shown in figure 24(a) as a function of Re_t . Although Re_t is varied from 140 to 370, Re_l remains approximately constant, giving evidence that this Reynolds number is the relevant local control parameter for the instability. The scatter is important, and is mainly due to the precision in the measurement of w , but the critical local Reynolds number can be estimated as

$$Re_{l,c} \approx 110 \pm 20. \quad (6.2)$$

This value is in qualitative agreement with the threshold $Re \approx 85 \pm 10$ measured by Rabaud & Couder (1983) from the circular shear layer experiment. Our slightly higher value may be due to the overestimation of the apparent shear layer thickness, or to some stabilizing effect due to the particular geometry of the annular shear layer. It is worth pointing out that, for the range of Reynolds number Re_t spanned here, the relative curvature of the shear layer, w/R_0 (where R_0 is the shear layer radius), increases from 0.16 to 0.52. However, this important variation does not significantly affect the threshold Re_l , suggesting that the curvature has only weak effect on the stability of this shear layer.

The approximate collapse of the onset curves in the plane of parameters $(\Gamma Re_t, \Gamma Re_b)$, observed in figure 10, follows from this constant Re_l at the onset. Taking $R_0\Omega_t$ as an estimate for the velocity jump ΔU , and using $w \sim h$ for the shear layer thickness, then the condition $Re_l = \Delta U w/\nu \approx \text{cste}$ simply yields $R_0 h \Omega_t/\nu = \Gamma Re_t (R_0/R) \approx \text{cste}$, confirming the experimental finding that the Reynolds numbers ΓRe_i are the most relevant global control parameters to describe the onset curves. However the link between Re_l and Re_t remains non trivial because of the additional ratio R_0/R , and accounts for the scatter in figure 10.

One consequence of this shear layer instability is that the critical wavelength should

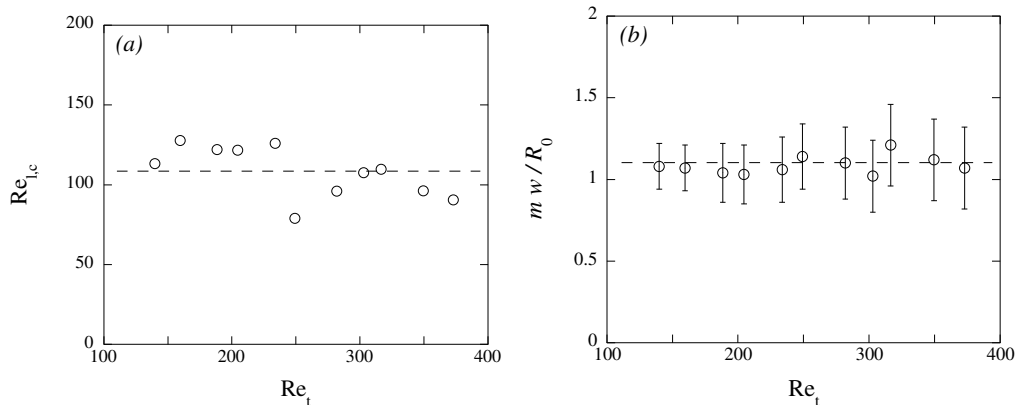


FIGURE 24. (a) Critical local Reynolds number $Re_{l,c}$ based on the shear layer thickness as a function of Re_t for $\Gamma = 7$. For each measurement, the bottom Reynolds number Re_b is fixed to its transition value. (b) Corresponding normalized wavenumber $m w / R_0$.

scale as the thickness w of the shear layer (Drazin & Reid 1979). As a result, the number of vortices along the shear layer is expected to scale as $2\pi R_0/w$, where $2\pi R_0$ is the total length of the shear layer. This is indeed the case, as shown in figure 24(b), where the normalized wavenumber $m w / R_0$ is plotted as a function of Re_t . The observed constant value,

$$\frac{m w}{R_0} \approx 1.10 \pm 0.15, \quad (6.3)$$

confirms this picture, leading to a wavelength

$$\lambda = 2\pi R_0 / m \approx (5.7 \pm 0.8)w. \quad (6.4)$$

Here again this finding compares well with the circular shear layer experiment of Rabaud & Couder (1983), for which the shear layer radius is constrained by the geometry of the apparatus. In the present rotating disks experiment, this radius R_0 is not fixed, but results from the competition of the centrifugal effects on each disk.

From the $m \propto R_0$ law observed here for $\Gamma = 7$, one may deduce that the onset mode is a decreasing function of Re_t , since the increasing centrifugal effect of the faster disk tends to decrease the radius of the shear layer R_0 . This is indeed the case (see, e.g., figure 12), at least for moderate aspect ratios Γ ; for higher aspect ratios the interaction with the boundary layers significantly affect this behaviour, as shown in the next section.

6.2. Onset modes

The observed modes are found to not only depend on the Reynolds numbers and the aspect ratio, but also on the time history of the control parameters (Re_b, Re_t), as shown in section 5.4. As a consequence, the only quantity that may be summarized is the critical mode that first get unstable just at the onset when slowly approaching the onset curve from below. This onset mode then coincides with the first unstable mode obtained from the linear computations.

Figure 25 shows the experimental regime diagram for the onset mode in the plane of parameters (Γ, Re_t) . For each value of the top Reynolds number, Re_t , the bottom Reynolds number, Re_b , has been fixed to its transition value (see figure 9). As noted in section 5.4, the sensitivity of the observed mode slightly beyond the onset curve is important (see figure 21), so that the observed mode m may occasionally surestimate the actual onset mode, shifting upwards the transition lines between modes.

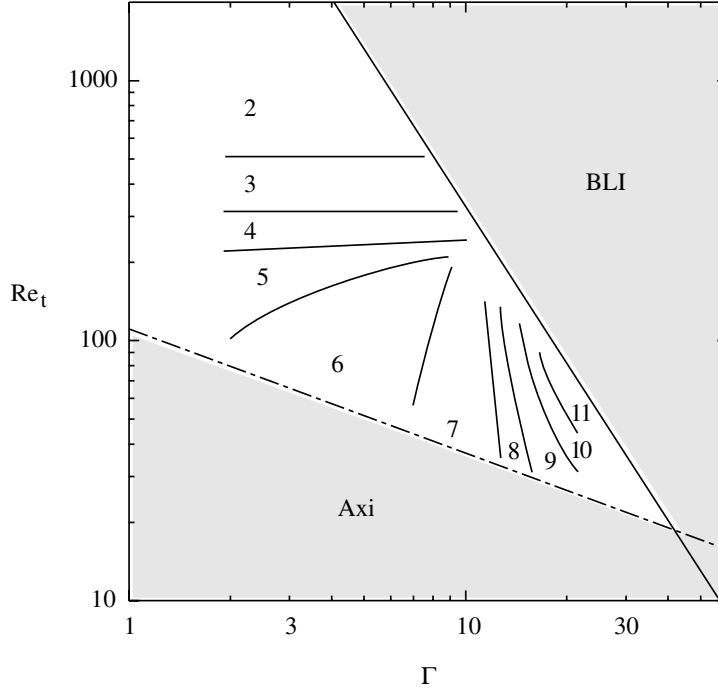


FIGURE 25. Experimental regime diagram of the onset modes in the plane (Γ, Re_t) , where $\Gamma = R/h$ is the aspect ratio and Re_t the top Reynolds number (the bottom Reynolds number, Re_b , is fixed to its transition value). Modes between $m = 2$ and 11 are observed, for Γ between 2 and 21. In the “Boundary layer instability” domain, noted *BLI* ($Re_t > 31 \times 10^3 \Gamma^{-2}$), boundary layer instabilities occur in addition to the shear layer instability, and are not described in the present study. In the lower domain, noted *Axi* ($Re_t < 105 \Gamma^{-1/2}$), the axisymmetric basic flow remains stable.

This diagram is restricted to a triangle in the plane (Γ, Re_t) . In the domain noted *Axi*, below a border line given by

$$Re_t \approx (105 \pm 9) \Gamma^{-1/2}, \quad (6.5)$$

the flow is found to remain axisymmetric. In this domain the shear layer is probably stabilized by the thick boundary layers that fill the entire vertical gap, but no simple argument is found to explain the observed $\Gamma^{-1/2}$ behaviour.

The domain above the upper border line, denoted *BLI* as “boundary layer instability”, corresponds to the destabilization of the inward boundary layer on the slower rotating disk. The associated instability patterns, axisymmetric propagating circles and positive spirals, have been described in details by Gauthier *et al.* (2002), and are not considered here. Since the boundary layer stability is controlled by a local Reynolds number, $Re_r = \Omega r^2 / \nu$, an approximate condition for stability is that $Re_r < Re_c$ for all $r < R$, leading to a border line $\Omega_t R^2 / \nu = Re_c$, or equivalently

$$Re_t = \Omega_t h^2 / \nu = Re_c \Gamma^{-2}. \quad (6.6)$$

This is indeed the case, and we determine experimentally $Re_c \approx (31 \pm 2) \times 10^3$. Note that although measurements of the critical mode were sometimes possible slightly beyond this upper limit, we choose to restrict to the situation where the boundary layers remain stable.

For high Reynolds number, $Re_t > 200$ (i.e. only for $\Gamma < 12$), the separating lines are

nearly horizontal, i.e. the critical mode m is essentially controlled by the top Reynolds number, Re_t , and takes values from 5 down to 2 as Re_t is increased. The corresponding flow pattern essentially consists of the sharp-cornered polygon, as seen in figure 8(a-c). The onset mode $m = 4$ reported by Lopez *et al.* (2002) for $(\Gamma, Re_t) = (2, 250)$ agrees with the $m = 4$ domain in figure 25, that extends between $Re_t = 230 \pm 10$ and 320 ± 20 . In this regime, the boundary layers over each disk are well separated, $\delta = (\nu/\Omega_t)^{1/2} < h/12$, so that the dynamics of the annular shear layer can be seen as essentially two-dimensional. The onset mode then only depends on the shear layer radius R_0 and thickness $\delta \sim h$, in agreement with the law $m \propto R_0$ observed in the previous section for $\Gamma = 7$ (equation 6.3). As a consequence, while the Reynolds number based on the azimuthal velocity, $\Gamma Re_t = Rh\Omega_t/\nu$, is the relevant control parameter for the instability threshold (see figure 10), the Reynolds number $Re_t = h^2\Omega_t/\nu$ is the one that controls the onset mode in the $Re_t > 200$ domain.

For lower Reynolds numbers, $Re_t < 200$, this behaviour does not hold any more and the regime diagram becomes much more complex. In this regime, the flow is fully three-dimensional, with thick boundary layers, $\delta > h/12$, that may strongly interact with the annular shear layer. The corresponding flow pattern now evolves towards the spiral arms of figure 8(d-f). As Γ is increased, the lines of mode transition are getting nearly vertical, and their slope becomes negative for $\Gamma > 12$. As a consequence, the critical mode now increases as the Reynolds number is increased, in contrast with the low aspect ratio case. This new behaviour is in agreement with the results of Gauthier *et al.* (2002) at $\Gamma = 20.9$, where modes 9, 10 and 11 were reported for increasing Reynolds numbers.

We finally note that extrapolating the border lines of the two domains *Axi* and *BLI* towards higher aspect ratio suggests that the shear layer instability described here should only be observed for $\Gamma < 40$. The present experiment being limited to $\Gamma = 20.9$, this upper bound has not been tested experimentally. For higher aspect ratio, the boundary layers would become unstable as soon as they get separated, probably inhibiting or strongly affecting the shear layer instability. Other instability mechanisms may also appear for such high aspect ratios, as the turbulent spots in the torsional Couette flow described by Cros & Le Gal (2002) in the rotor-stator configuration.

6.3. Phase velocities

Because of the asymmetry of the flow, the instability patterns are not steady, but rather appear as rotating waves, characterized by a well defined drift velocity ω . Figure 26 shows the experimentally measured angular phase velocity at the onset, ω , normalized by the top angular velocity, Ω_t , as a function of Re_t for various aspect ratios. Although the scatter is important, the different curves appear to collapse reasonably well. The phase velocity is found to increase, starting from slightly negative values for low Re_t , crossing zero for $Re_t \sim 50 - 100$, and finally saturating towards a constant positive value for $Re_t > 250$,

$$\frac{\omega}{\Omega_t} \approx 0.095 \pm 0.01. \quad (6.7)$$

For high Reynolds numbers, the shear layer can be seen as essentially two-dimensional, with no significant effect of the boundary layers. The constant phase velocity ω/Ω_t observed in this case is similar to the classical linear Kelvin-Helmholtz case, for which the phase velocity is given by the average of the two stream velocities, $\Delta U = (U_1 + U_2)/2$ (Drazin & Reid 1979). Extending this result for the annular case yields $\omega = (\Omega_1 + \Omega_2)/2$, where Ω_1 and Ω_2 are respectively the inner and outer angular velocities on each side of the shear layer. These angular velocities are non trivial functions of the bottom and top disk velocities, Ω_b and Ω_t . However, a rough estimate for ω may be obtained by

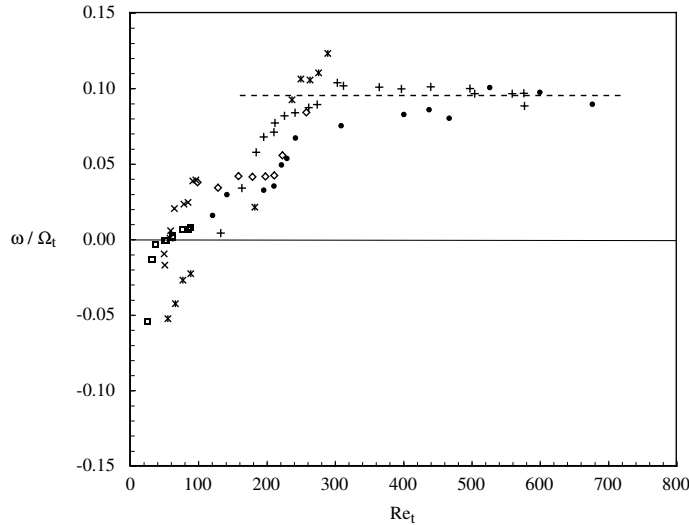


FIGURE 26. Normalized phase velocity ω/Ω_t at the onset as a function of Re_t for various aspect ratios Γ . \diamond : 3. \bullet : 5.2. $+$: 7. $*$: 9.3. \times : 17. \square : 20.9. The dashed line is $\omega/\Omega_t = 0.095$.

neglecting Ω_1 , and taking $\Omega_2 \approx 0.3\Omega_t$ as for the classical Batchelor flow (see figure 23). These approximations yield $\omega/\Omega_t \approx 0.3/2 \approx 0.15$, which is in reasonable agreement with the observed limit, $\omega/\Omega_t \approx 0.095 \pm 0.01$.

The much lower values for ω found in the lower Reynolds number regime, $Re_t < 250$, is the result of the interaction with the boundary layers, which tend to slow down the pattern rotation. This slowing down probably originates from the upward flow in the region of the shear layer, which brings low angular momentum from the slower disk into the bulk of the flow.

7. Conclusion

This paper describes a joint laboratory and numerical study of the instability patterns in the flow between counter-rotating disks, spanning a range of aspect ratio $\Gamma = R/h$ between 2 and 21. This study is restricted to the situation where the boundary layers remain stable, focusing on the shear layer instability that occurs only in the counter-rotating regime. The associated pattern is a combination of a sharp-cornered polygonal shear layer with m vorticity extrema, surrounded by a set of m inner and $2m$ outer spiral arms. At small aspect ratio Γ and/or large velocity, only the m -sided polygon is observed, where the mode m decreases as the Reynolds number is increased. On the other hand, for higher Γ and/or smaller velocity, only the spiral arms remain, the number of which now increasing as the Reynolds number is increased. These observations are in remarkable agreement with the three-dimensional numerical simulations performed for the same values of the parameters (Γ , Re_t , Re_b).

Onset curves have been experimentally determined for various aspect ratios. Their collapse into a single master curve when plotted in the plane of parameters (ΓRe_t , ΓRe_t) provides good indication that the two patterns originate from the same instability mechanism, namely a free shear layer instability. This shear layer separates an outer region rotating with the faster disk from an inner region where very low velocity takes place, and is a peculiarity of the flow between counter-rotating disks. For sufficiently large counter-rotation, this shear layer is strengthened by the presence of a stagnation circle on the

slower rotating disk. As a consequence, the instability usually arises when the stagnation circle is present, except for the highest aspect ratio, around $\Gamma > 16$, where the instability may slightly anticipate the onset of the two-cell recirculation structure.

Focusing on the low aspect ratio case, $\Gamma < 10$, where PIV measurements are possible, we further characterized the instability in terms of local Reynolds number Re_l based on the shear layer thickness w . The constant value of this Reynolds number at the onset of the instability, $Re_{l,c} \approx 110 \pm 20$, confirms that the transition originates from a shear layer instability. Consequently, the critical mode m scales as R_0/w , where R_0 is the radius of the annular shear, which results from the competition between the centrifugal effects of each disk. In other words, the instability patterns can be seen as a set of vortices of size $\sim w$ regularly filling the shear layer perimeter. As a result, the onset mode is a decreasing function of the Reynolds number, since the shear layer radius decreases as the faster disk becomes more dominant. Finally, it is shown that the normalized phase velocity, ω/Ω_t , is an increasing function of the Reynolds number that tends towards a constant value for high Re_t .

All these findings indicate that this instability of the flow between counter-rotating disks can simply be described in terms of a classical Kelvin-Helmholtz instability, where curvature has only weak effect, and that the surrounding spiral arms result from the interaction of this unstable shear layer with the Ekman boundary layers over the faster disk. These observations for various aspect ratios reveals the continuity between the patterns observed by Lopez *et al.* (2002) and Marques *et al.* (2003) for $\Gamma \leq 2$ and the “negative spirals” of Gauthier *et al.* (2002) for $\Gamma = 20.9$. These patterns may also be compared to the ones recently reported by Nore *et al.* (2003*a, b*) for Γ between 1/3 and 2 in the exact-counter-rotating flow with a stationary sidewall. The higher degree of symmetry of this latter flow leads to a strictly equatorial layer giving rise to radial steady co-rotating vortices.

We gratefully acknowledge G. Gauthier, P. Gondret, G.M. Homsy, C. Nore, L. S. Tuckerman and J.E. Wesfreid for fruitful discussions. We are indebted to G. Chauvin, R. Pidoux and C. Saurine for experimental helps. The computations were carried out on the NEC-SX5 computer of the Institut du Développement et des Ressources en Informatique Scientifique (IDRIS) of the Centre National pour la Recherche Scientifique (CNRS) (project no. 0327).

REFERENCES

- BATCHELOR, G. K. 1951 Note on a class of solutions of the Navier–Stokes equations representing steady rotationally-symmetric flow. *Q. J. Mech. Appl. Maths* **4**, 29–41.
- BARBOSA, E. & DAUBE, O. 2001 A Finite Differences Method in Cylindrical Coordinates for 3D Incompressible Flows. ECCOMAS CFD Conference, Swansea, UK.
- BERGERON, K., COUSIAS, E.A., LYNOV, J.P., & NIELSEN, A.H. 2000 Dynamical properties of forced shear layers in an annular geometry. *J. Fluid Mech.* **402**, 255–289.
- BLACKBURN, H. M. & LOPEZ, J. M. 2002 Modulated rotating waves in an enclosed swirling flow. *J. Fluid Mech.* **465**, 33–58.
- BÖDEWADT, U. T. 1940 Die Drehströmung über festem Grund. *Z. Angew. Math. Mech.* **20**, 241–253.
- CHOMAZ, J.M., RABAUD, M., BASDEVANT, C. & COUDER, Y. 1988 Experimental and numerical investigation of a forced circular shear layer. *J. Fluid Mech.* **187**, 115–140.
- CROS, A. & LE GAL, P. 2002 Spatiotemporal intermittency in the torsional Couette flow between a rotating and a stationary disk. *Phys. Fluids* **14**, 3755–3765.
- DAUBE, O., & LE QUÉRÉ, P. 2002 Numerical investigation of the first bifurcation for the flow in a rotor-stator cavity of radial aspect ratio 10. *Computers & Fluids* **31**, 481–494.

- DIJKSTRA, D. & VAN HEIJST, G.J.F. 1983 The flow between finite rotating disks enclosed by a cylinder. *J. Fluid Mech.* **128**, 123–154.
- DOLZHANSKII, F.V., KRYMOV, V.A. & MANIN, D. YU 1990 Stability and vortex structures of quasi-two-dimensional shear flows. *Sov. Phys. Usp* **33** (7), 495–520.
- DRAZIN, P.G. & REID, W.H. 1979 *Hydrodynamic instability*. Cambridge University Press.
- ESCUDIER, M.P. 1984 Observations of the flow produced in a cylindrical container by a rotating end wall. *Exps. Fluids* **2**, 179–186.
- FRÜH, W.G. & READ, P.L. 1999 Experiments on a barotropic rotating shear layer. Part 1. Instability and steady vortices. *J. Fluid Mech.* **383**, 143–173.
- GADOIN, E., LE QUÉRÉ, P. & DAUBE O. 2001 A General Methodology to Investigate Flow Instabilities in Complex Geometries: Application to Natural Convection in Enclosures. *Int. J. Num. Meth. in Fluids* **37**, 175–208.
- GAUTHIER, G., GONDRET, P. & RABAUD, M. 1998 Motions of anisotropic particles: application to visualization of three-dimensional flows. *Phys. Fluids* **10**, 2147–2154.
- GAUTHIER, G., GONDRET, P. & RABAUD, M. 1999 Axisymmetric propagating vortices in the flow between a stationary and a rotating disk enclosed by a cylinder *J. Fluid Mech.* **386**, 105–126.
- GAUTHIER, G., GONDRET P., MOISY, F. & RABAUD, M. 2002 Instabilities in the flow between co and counter-rotating disks. *J. Fluid Mech.* **473**, 1–21.
- GELFGAT, A. Y., BAR-YOSEPH, P. Z. & SOLAN, A. 2001 Three-dimensional instability flow in a rotating lid–cylinder enclosure. *J. Fluid Mech.* **438**, 363–377.
- GODA, K. 1979 A multistep technique with implicit difference schemes for calculating two or three dimensional cavity flows. *J. Comp. Phys.* **30**, 76–95.
- HIDE, R. & TITMAN, C.W. 1967 Detached shear layers in a rotating fluid. *J. Fluid. Mech.* **29**, 39–60.
- HUMPHREY, J.A.C., SCHULER C.A. & WEBSTER D.R. 1995 Unsteady laminar-flow between a pair of disks corotating in a fixed cylindrical enclosure. *Phys. Fluids* **7** (6), 1225–1240.
- HYMAN, J.M. & SHASHKOV, M. 1997 Natural discretization for the divergence, gradient and curl on logically rectangular grids. *Comp. Math. Appl.* **33**, 81–104.
- KÁRMÁN VON, T. 1921 Laminar und turbulente reibung. *Z. Angew. Math.* **1**, 233–252.
- KONIJNENBERG, J.A. VAN DE, NIELSEN, A.H., RASMUSSEN, J.J. & STENUM, B. 1999 Shear flow instability in a rotating fluid. *J. Fluid. Mech.* **387**, 177–204.
- LIU, W.W. 1994 Linear instability of curved free shear layers. *Phys. Fluids* **6** (2), 541–549.
- LOPEZ, J. M. 1998 Characteristics of endwall and sidewall boundary layers in a rotating cylinder with a differentially rotating endwall. *J. Fluid. Mech.* **359**, 49–79.
- LOPEZ, J.M., HART, J.E., MARQUES, F. KITTELMAN, S. & SHEN, J. 2002 Instability and mode interactions in a differentially-driven rotating cylinder. *J. Fluid. Mech.* **462**, 383–409.
- MAMUM, C.K. & TUCKERMAN, L.S. 1995 Asymmetry and Hopf bifurcation in spherical Couette flow. *Phys. Fluids* **7**, 80–91.
- MARQUES, F., GELFGAT, A. YU., LOPEZ, J.M. 2003 Tangent double Hopf bifurcation in a differentially rotating cylinder flow. *Phys. Rev. E* **68**, 016310, 1–13.
- MOISY, F., PASUTTO, T., & RABAUD, M. 2003 Instability patterns between counter-rotating disks. *Nonlinear Processes in Geophysics* **10**, 281–288.
- NIINO, H. & MISAWA, N. 1984 An experimental and theoretical study of barotropic instability. *J. Atmos. Sci.* **41**, 1992–2011.
- NORE, C., TUCKERMAN, L.S., DAUBE, O., & XIN, S. 2003a The 1:2 mode interaction in exactly counter-rotating von Kármán swirling flow. *J. Fluid. Mech.* **477**, 51–88.
- NORE, C., TARTAR, M., DAUBE, O. & TUCKERMAN, L.S. 2003b Survey of instability thresholds of flow between exactly counter-rotating disks. *subm. to J. Fluid. Mech.*
- OTTO, S.R., JACKSON, T.L., & HU, F.Q. 1996 On the spatial evolution of centrifugal instabilities within curved incompressible mixing layers. *J. Fluid. Mech.* **315**, 85–103.
- RABAUD, M. & COUDER, Y. 1983 Instability of an annular shear layer. *J. Fluid. Mech.* **136**, 291–319.
- SAAD, Y. & SCHULTZ, M.H. 1986 GMRES: a generalized minimal residual algorithm for solving nonsymmetric linear systems. *S.I.A.M. J. Sci. Stat. Comput.* **7**, 856–869.
- SAVAS, Ö. 1985 On flow visualization using reflective flakes. *J. Fluid. Mech.* **152**, 235–248.

- SCHOUVEILER, L., LE GAL, P. & CHAUVE, M.-P. 2001 Instabilities of the flow between a rotating and stationary disk. *J. Fluid Mech.* **443**, 329–350.
- SERRE, E., CRESPO DEL ARCO, E. & BONToux, P. 2001 Annular and spiral patterns in flows between rotating and stationary discs. *J. Fluid Mech.* **434**, 65–100.
- SERRE, E. & BONToux, P. 2002 Vortex breakdown in a three-dimensional swirling flow. *J. Fluid Mech.* **459**, 347–370.
- STEWARTSON, K. 1953 On the flow between two rotating coaxial disks. *Proc. Camb. Phil. Soc.* **49**, 333–341.
- TUCKERMAN, L.S. 1989 Steady-state solving via Stokes preconditioning: Recurrence relations for elliptic operators. *Lecture notes in Physics*, edited by D.L. Dwoyer, M.Y. Hussaini, and R.G. Voigt, Springer, New York, 573–577.
- YANASE, S., FLORES, C., MÉTAIS, O. & RILEY, J.J. 1993 Rotating free-shear flows. I. Linear stability analysis *Phys. Fluids A* **5**, (11) 2725–2737.
- ZANDBERGEN, P.J. & DIJKSTRA, D. 1987 Von Kármán swirling flows. *Ann. Rev. Fluid Mech.* **19**, 465–91.